

# Atmospheres and spectra of strongly magnetized neutron stars

Wynn C. G. Ho<sup>★</sup> and Dong Lai<sup>★</sup>

*Center for Radiophysics and Space Research, Department of Astronomy, Cornell University Ithaca, NY 14853, USA*

Accepted 2001 July 2. Received 2001 June 27; in original form 2001 April 18

## ABSTRACT

We construct atmosphere models for strongly magnetized neutron stars with surface fields  $B \sim 10^{12}$ – $10^{15}$  G and effective temperatures  $T_{\text{eff}} \sim 10^6$ – $10^7$  K. The atmospheres directly determine the characteristics of thermal emission from isolated neutron stars, including radio pulsars, soft gamma-ray repeaters, and anomalous X-ray pulsars. In our models, the atmosphere is composed of pure hydrogen or helium and is assumed to be fully ionized. The radiative opacities include free–free absorption and scattering by both electrons and ions computed for the two photon polarization modes in the magnetized electron–ion plasma. Since the radiation emerges from deep layers in the atmosphere with  $\rho \gtrsim 10^2 \text{ g cm}^{-3}$ , plasma effects can significantly modify the photon opacities by changing the properties of the polarization modes. In the case where the magnetic field and the surface normal are parallel, we solve the full, angle-dependent, coupled radiative transfer equations for both polarization modes. We also construct atmosphere models for general field orientations based on the diffusion approximation of the transport equations and compare the results with models based on full radiative transport. In general, the emergent thermal radiation exhibits significant deviation from blackbody, with harder spectra at high energies. The spectra also show a broad feature ( $\Delta E/E_{Bi} \sim 1$ ) around the ion cyclotron resonance  $E_{Bi} = 0.63(Z/A)(B/10^{14} \text{ G}) \text{ keV}$ , where  $Z$  and  $A$  are the atomic charge and atomic mass of the ion, respectively; this feature is particularly pronounced when  $E_{Bi} \gtrsim 3kT_{\text{eff}}$ . Detection of the resonance feature would provide a direct measurement of the surface magnetic fields on magnetars.

**Key words:** magnetic fields – radiative transfer – stars: atmospheres – stars: magnetic fields – stars: neutron – X-rays: stars.

## 1 INTRODUCTION

Neutron stars (NSs) are created in the core collapse and subsequent supernova explosion of massive stars and begin their lives at high temperatures,  $T \gtrsim 10^{11}$  K. As they cool over the next  $\sim 10^5$ – $10^6$  yr, they act as sources of soft X-rays with surface temperatures  $\gtrsim 10^5$  K. The cooling history of the NS depends on poorly constrained interior physics such as the nuclear equation of state, superfluidity, and magnetic field (see, e.g., Tsuruta 1998; Yakovlev et al. 2001, for a review). Thus observations of surface emission from isolated NSs can provide invaluable information on the physical properties and evolution of NSs. In recent years, the spectra of several radio pulsars (e.g. PSR B1055–52, B0656+14, and Geminga) have been observed to possess a thermal component that can be attributed to the surface emission at temperatures in the range  $(2\text{--}10) \times 10^5$  K, while a few other pulsars show thermal emission from hot spots at temperatures of a few times  $10^6$  K on the NS surface (e.g., for observations in the X-rays, see Becker &

Trümper 1997; Becker 2000; in the extreme ultraviolet, Edelstein, Foster & Bowyer 1995; Korpela & Bowyer 1998; in the optical band, Pavlov, Welty & Cordova 1997; Caraveo et al. 2000). In addition, several radio-quiet, isolated NSs, presumably accreting from the interstellar medium (see Treves et al. 2000), have been detected in the X-ray and optical bands (e.g. Caraveo, Bignami & Trümper 1996; Walter, Wolk & Neuhäuser 1996; Walter & Matthews 1997; Caraveo 1998; Mignani, Caraveo & Bignami 1998; Paerels et al. 2001). Recent observations by the *Chandra* X-ray Observatory have also revealed a number of compact central sources in supernova remnants with spectra consistent with thermal emission from isolated NSs (see Pavlov 2000). Most interestingly, in the last few years, thermal radiation has been detected from a potentially new class of NSs, ‘magnetars’, which possess superstrong magnetic fields ( $B \gtrsim 10^{14}$  G) (Duncan & Thompson 1992; Thompson & Duncan 1993, 1995, 1996; see Thompson 2000 for a review).

Observations of soft gamma-ray repeaters (SGRs) and anomalous X-ray pulsars (AXPs) strongly suggest that these are NSs endowed with superstrong magnetic fields (e.g. Vasisht & Gotthelf 1997; Kouveliotou et al. 1998, 1999; see, e.g., Hurley

<sup>★</sup>E-mail: wynrho@astro.cornell.edu (WCGH); dong@astro.cornell.edu (DL)

2000 for SGR review; Mereghetti 1999 for AXP review). According to the magnetar model, the X-ray luminosity from AXPs and the quiescent X-ray emission from SGRs are powered by the decay of a superstrong ( $B \sim 10^{14}$ – $10^{15}$  G) magnetic field (Thompson & Duncan 1996) and/or by the residual thermal energy (Heyl & Hernquist 1997a). Alternatively, it has been proposed that the AXP emission may originate from accretion on to a NS with  $B \sim 10^{12}$  G, e.g., from a fossil disc left over from the supernova explosion (see Alpar 2001; Chatterjee, Hernquist & Narayan 2000, and references therein). However, detailed timing studies of AXPs and SGRs (e.g. Thompson et al. 2000; Kaspi et al. 2001) and deep optical observations (e.g. Hulleman, van Kerkwijk & Kulkarni 2000; Kaplan et al. 2001), as well as the many similarities between AXPs and SGRs, clearly favour the magnetar model for both AXPs and SGRs. Nevertheless, it should be emphasized that, like radio pulsars, the magnetic field strengths ( $B \sim 10^{14}$ – $10^{15}$  G) of magnetars are indirectly inferred and are based on the measurement of the spin periods (6–12 s) and period derivatives and on the assumption that the spin-down is because of the loss of angular momentum that is carried away by magnetic dipole radiation or Alfvén waves (Thompson & Blaes 1998; Thompson et al. 2000). Thermal radiation has already been detected in four of the five AXPs (1E 1048.1–5937, 1E 1845–0258, 4U0142+61, RXS J1708–40) and in SGR 1900+14; fits to the spectra with blackbody or with crude atmosphere models indicate that the thermal X-rays can be attributed to magnetar surface emission at temperatures of  $(3\text{--}7) \times 10^6$  K (see Mereghetti 1999; Perna et al. 2001). Clearly, detailed observational and theoretical studies of thermal emission can potentially reveal much about the physical conditions and the true nature of magnetars. Of particular importance are possible spectral features, such as the ion cyclotron line (see equation 1.1) studied in this paper (see also Zane et al. 2001), which, if detected, can provide a direct measurement of the surface magnetic field. In fact, it has been suggested that the lack of proton and electron cyclotron features in *XMM-Newton* observations of the isolated NS RX J0720.4–3125 may lead to constraints on its surface magnetic field (Paerels et al. 2001).

Thermal radiation from a magnetized NS is mediated by the thin atmospheric layer (with scaleheight  $\sim 0.1$ – $10$  cm and density  $\sim 0.1$ – $100$  g cm $^{-3}$ ) that covers the stellar surface. The physical properties of the atmosphere, such as the chemical composition, equation of state, and especially the radiative opacities, directly determine the characteristics of the thermal emission. While the surface composition of the NS is unknown, a great simplification arises because of the efficient gravitational separation of light and heavy elements (with time-scales of the order of seconds; see Alcock & Illarionov 1980 for a discussion of gravitational separation in white dwarfs). A pure H atmosphere is expected even if a small amount of fallback/accretion occurs after NS formation.<sup>1</sup> A pure He atmosphere results if H is completely burnt up, and a pure Fe atmosphere may be possible if no fallback/accretion occurs.

Steady progress has been made over the years in modelling NS atmospheres. The first models of zero-field NS atmospheres were constructed by Romani (1987). Later works used improved opacity and equation of state data from the OPAL project for pure hydrogen, helium, and iron compositions (Rajagopal & Romani 1996; Zavlin, Pavlov & Shibano 1996). These works showed that

the radiation spectra from light element (H or He), low-field ( $B \lesssim 10^8$  G) atmospheres deviate significantly from blackbody spectra. Magnetic NS atmosphere modelling was first attempted by Miller (1992), who unfortunately adopted an incorrect polarization-averaging procedure for the radiative transport and included only bound-free opacities. So far the most comprehensive studies of magnetic NS atmospheres have focused on hydrogen and moderate field strengths of  $B \sim 10^{12}$ – $10^{13}$  G (Shibano et al. 1992; Pavlov et al. 1994; see Pavlov et al. 1995 for a review and Zane, Turolla & Treves 2000 for full, angle-dependent atmosphere models with accretion). These models correctly take into account the transport of different photon modes (in the diffusion approximation) through a mostly ionized medium. The opacities adopted in the models include free–free transitions and electron scattering, while bound-free opacities are treated in a highly approximate manner and bound–bound transitions are completely ignored. Because the strong magnetic field significantly increases the binding energies of atoms, molecules, and other bound states (see Lai 2001 for a recent review), these bound states have appreciable abundances in the atmosphere at low temperatures ( $T \lesssim 10^6$  K) (see Lai & Salpeter 1997; Potekhin, Chabrier & Shibano 1999). Therefore the models of Pavlov et al. are expected to be valid only for relatively high temperatures ( $T \gtrsim \text{a few} \times 10^6$  K), where hydrogen is almost completely ionized. The presence of a magnetic field gives rise to anisotropic and polarized emission from the atmosphere (see Pavlov & Zavlin 2000). The resulting magnetic spectra are softer at X-ray energies than the low-field spectra but are still harder than the blackbody spectra. Models of magnetic iron atmospheres (with  $B \sim 10^{12}$  G) were studied by Rajagopal, Romani & Miller (1997). Because of the complexity in the atomic physics and radiative transport, these Fe models are necessarily crude. Despite a number of shortcomings, these H and Fe atmosphere models have played a valuable role in assessing the observed spectra of several radio pulsars and radio-quiet NSs (e.g., it is now well recognized that fitting the thermal spectra by a blackbody in the X-rays tends to overestimate the effective temperature) and some useful constraints on NS properties have been obtained (e.g. Meyer, Pavlov & Mészáros 1994; Pavlov et al. 1996; Zavlin, Pavlov & Trümper 1998).

This paper is the first in a series where we systematically investigate the atmosphere and spectra of strongly magnetized NSs. Here we study the H and He atmospheres with relatively high effective temperatures ( $T_{\text{eff}} \gtrsim \text{a few} \times 10^6$  K) so that bound atoms or molecules may be neglected. We focus on the superstrong field regime ( $B \gtrsim 10^{14}$  G) and compare with results from models possessing weaker magnetic fields. We construct self-consistent atmosphere models in radiative equilibrium and solve the full, angle-dependent, coupled transport equations for both polarization modes. For comparisons, we also study models based on the diffusion approximation of the transport equations. Of particular interest is the effect of the ion cyclotron resonance, which occurs at energy

$$E_{Bi} = \hbar\omega_{Bi} = \hbar \frac{ZeB}{Am_p c} = 0.63 \left( \frac{Z}{A} \right) \left( \frac{B}{10^{14} \text{ G}} \right) \text{ keV}, \quad (1.1)$$

where  $Z$  and  $A$  are the charge number and mass number of the ion, respectively. As we show in this paper, the resonance gives rise to a broad ( $\Delta E/E \sim 1$ ) spectral feature around  $E_{Bi}$ , and this feature is particularly pronounced when  $E_{Bi} \gtrsim 3kT_{\text{eff}}$ . Obviously, the ion cyclotron feature can potentially provide important diagnostics for the physical properties of magnetars.

<sup>1</sup> As far as the radiation spectrum is concerned, the photons decouple from the matter at Thomson depth  $\tau \lesssim 10^3$  (see Fig. 5); the total mass above this depth is less than  $10^{16}$  g.

While in the final stages of writing our paper for publication, we became aware of two recent papers that also explore H atmospheres in the superstrong field regime. Özel (2001) included the effect of vacuum polarization (see Section 5) but neglected the ion effect on both opacities and polarization modes, while Zane et al. (2001) studied the proton cyclotron feature and adopted an approximate description of the polarization modes in the electron–proton plasma with vacuum polarization (see also Section 5).

In Section 2, we review the basic physics ingredients of our atmosphere models, including the radiative transfer equations (RTEs), the equation of state, and the opacities. The numerical methods for both full transport and diffusion models and tests of the solution are discussed in Section 3. In Section 4, we present our numerical atmosphere models and spectra for different compositions (H or He), effective temperatures, and magnetic field strengths and geometries. Finally, Section 5 contains a discussion of the uncertainties in our models and possible future works.

## 2 ATMOSPHERE MODEL: BASIC EQUATIONS AND PHYSICS INPUTS

We consider an isolated NS with a plane-parallel atmosphere. This is justified since the atmospheric scaleheight  $H \lesssim 10$  cm is much less than the NS radius  $R \approx 10$  km. The atmosphere is composed of pure hydrogen or helium (see Section 1). The temperature  $T$  is taken to be  $\gtrsim 10^6$  K, and the atmosphere is assumed to be fully ionized (see Section 5 for discussion on ionization equilibrium). A uniform magnetic field  $\mathbf{B}$  permeates the atmosphere, and the angle between the direction of the magnetic field  $\hat{\mathbf{B}}$  and the surface normal  $\hat{\mathbf{z}}$  is  $\Theta_B$ .

### 2.1 Radiative Transfer Equation

In a magnetized plasma, there are two normal modes of propagation for electromagnetic waves. These are the extraordinary mode (X-mode,  $j = 1$ ), which is mostly polarized perpendicular to the  $\mathbf{k}$ – $\mathbf{B}$  plane, and the ordinary mode (O-mode,  $j = 2$ ), which is mostly polarized parallel to the  $\mathbf{k}$ – $\mathbf{B}$  plane, where  $\mathbf{k}$  is the unit vector along the wave propagation direction (e.g. Mészáros 1992; see Section 2.5). When the normal modes are approximately orthogonal and their relative phase shift over a mean free path is large (i.e. large Faraday depolarization), the radiative transfer of the four Stokes parameters reduces to that of the two modes (see Gnedin & Pavlov 1974). The RTE for the specific intensity  $I_\nu^j$  of mode  $j$  is

$$\mathbf{k} \cdot \nabla I_\nu^j(\mathbf{k}) = \rho \kappa_j^{\text{abs}}(\mathbf{k}) \frac{B_\nu}{2} - \rho \kappa_j^{\text{tot}}(\mathbf{k}) I_\nu^j(\mathbf{k}) + \rho \sum_{i=1}^2 \int d\mathbf{k}' \frac{d\kappa^{\text{sc}}(\mathbf{k}'i \rightarrow \mathbf{k}j)}{d\Omega} I_\nu^i(\mathbf{k}'), \quad (2.1)$$

where  $B_\nu = B_\nu(T)$  is the blackbody intensity,  $\kappa_j^{\text{abs}}(\mathbf{k})$  (in  $\text{cm}^2 \text{g}^{-1}$ ) is the absorption opacity (corrected for stimulated emission) for mode  $j$  propagating along  $\mathbf{k}$ ,  $d\kappa^{\text{sc}}(\mathbf{k}'i \rightarrow \mathbf{k}j)/d\Omega$  is the differential opacity for scattering from mode  $i$  in direction  $\mathbf{k}'$  to mode  $j$  in direction  $\mathbf{k}$ ,  $\kappa_j^{\text{tot}}(\mathbf{k}) = \kappa_j^{\text{abs}}(\mathbf{k}) + \kappa_j^{\text{sc}}(\mathbf{k})$  is the total opacity, and

$$\kappa_j^{\text{sc}}(\mathbf{k}) = \sum_{i=1}^2 \kappa_{ji}^{\text{sc}}(\mathbf{k}) \quad (2.2)$$

$$\kappa_{ji}^{\text{sc}}(\mathbf{k}) = \int d\mathbf{k}' \frac{d\kappa^{\text{sc}}(\mathbf{k}j \rightarrow \mathbf{k}'i)}{d\Omega'}. \quad (2.3)$$

Defining the Thomson depth  $\tau$  by  $d\tau = -\rho \kappa_0^{\text{es}} dz$ , where  $\kappa_0^{\text{es}} = Y_e \sigma_T / m_p = 0.4 Y_e \text{cm}^2 \text{g}^{-1}$  is the Thomson electron scattering opacity in the absence of a magnetic field and  $Y_e = Z/A$  is the electron fraction, equation (2.1) becomes

$$\mu \frac{\partial I_\nu^j(\mathbf{k})}{\partial \tau} = \frac{\kappa_j^{\text{tot}}(\mathbf{k})}{\kappa_0^{\text{es}}} I_\nu^j(\mathbf{k}) - \frac{\kappa_j^{\text{abs}}(\mathbf{k}) B_\nu}{\kappa_0^{\text{es}} 2} - \frac{1}{\kappa_0^{\text{es}}} \sum_{i=1}^2 \int d\mathbf{k}' \frac{d\kappa^{\text{sc}}(\mathbf{k}'i \rightarrow \mathbf{k}j)}{d\Omega} I_\nu^i(\mathbf{k}'), \quad (2.4)$$

where  $\mu \equiv \mathbf{k} \cdot \hat{\mathbf{z}} = \cos \theta$ . In general, at a given frequency  $\nu$  and depth  $\tau$ , the intensity  $I_\nu^j(\mathbf{k})$  depends on  $\mu$  and the azimuthal angle  $\phi$  when  $\mathbf{B}$  is not along the surface normal, i.e., when  $\Theta_B \neq 0$ . In solving the RTE, it is useful to introduce the two quantities

$$i_\nu^j(\mathbf{k}) = \frac{1}{2} [I_\nu^j(\mathbf{k}) + I_\nu^j(-\mathbf{k})] \quad (2.5)$$

and

$$f_\nu^j(\mathbf{k}) = \frac{1}{2} [I_\nu^j(\mathbf{k}) - I_\nu^j(-\mathbf{k})], \quad (2.6)$$

which are evaluated only for  $\mu \geq 0$  and are related to the mean specific intensity and energy flux (see Mihalas 1978 for the non-magnetic case). As a result, the RTE becomes

$$f_\nu^j(\mathbf{k}) = \mu \frac{\partial i_\nu^j(\mathbf{k})}{\partial \tau_\nu} \quad (2.7)$$

$$\mu \frac{\partial f_\nu^j(\mathbf{k})}{\partial \tau_\nu} = \mu^2 \frac{\partial^2 i_\nu^j(\mathbf{k})}{\partial \tau_\nu^2} = i_\nu^j(\mathbf{k}) - \frac{\kappa_j^{\text{abs}}(\mathbf{k}) B_\nu}{\kappa_j^{\text{tot}}(\mathbf{k}) 2} - \frac{2}{\kappa_j^{\text{tot}}(\mathbf{k})} \sum_{i=1}^2 \int_+ d\mathbf{k}' \frac{d\kappa^{\text{sc}}(\mathbf{k}'i \rightarrow \mathbf{k}j)}{d\Omega} i_\nu^i(\mathbf{k}'), \quad (2.8)$$

where  $d\tau_\nu = -\rho \kappa_j^{\text{tot}}(\mathbf{k}) dz$  is the total optical depth and  $\int_+$  implies that the domain of integration is restricted to  $\mathbf{k}' \cdot \hat{\mathbf{z}} = \mu' \geq 0$ . In deriving these equations, we have used the reflection symmetry of the opacities, i.e.  $\kappa_j^{\text{tot}}(\mathbf{k}) = \kappa_j^{\text{tot}}(-\mathbf{k})$  and  $d\kappa^{\text{sc}}(\mathbf{k}'i \rightarrow \mathbf{k}j)/d\Omega = d\kappa^{\text{sc}}(\mathbf{k}j \rightarrow \mathbf{k}'i)/d\Omega$ . The boundary conditions for the RTE are  $I_\nu^j(\mathbf{k}) = 0$  for  $\mu < 0$  at  $\tau_\nu = 0$  and  $I_\nu^j(\mathbf{k}) \rightarrow B_\nu/2$  at  $\tau_\nu \rightarrow \infty$ . In terms of  $i_\nu^j$ , these are

$$\mu \frac{\partial i_\nu^j}{\partial \tau_\nu} = i_\nu^j \quad \text{at } \tau_\nu = 0 \quad (2.9)$$

and

$$\mu \frac{\partial i_\nu^j}{\partial \tau_\nu} + i_\nu^j = \frac{1}{2} \left( \mu \frac{\partial B_\nu}{\partial \tau_\nu} + B_\nu \right) \quad \text{at } \tau_\nu \rightarrow \infty. \quad (2.10)$$

To obtain the constraint imposed by radiative equilibrium, we integrate the RTE (2.1) over the solid angle, which yields the zeroth-order moment of the transfer equation,

$$\nabla \cdot \mathbf{F}_\nu^j(\mathbf{k}) = \rho \int d\mathbf{k} \kappa_j^{\text{abs}}(\mathbf{k}) \frac{B_\nu}{2} - \rho \int d\mathbf{k} \kappa_j^{\text{tot}}(\mathbf{k}) I_\nu^j(\mathbf{k}) + \rho \sum_{i=1}^2 \int d\mathbf{k} \int d\mathbf{k}' \frac{d\kappa^{\text{sc}}(\mathbf{k}'i \rightarrow \mathbf{k}j)}{d\Omega} I_\nu^i(\mathbf{k}'), \quad (2.11)$$

where the specific energy flux of mode  $j$  is

$$\mathbf{F}_\nu^j \equiv \int d\mathbf{k} \mathbf{k} I_\nu^j(\mathbf{k}) = 2 \int_+ d\mathbf{k} \mathbf{k} f_\nu^j(\mathbf{k}). \quad (2.12)$$

In radiative equilibrium, the total flux,  $\mathbf{F} = \sum_{j=1}^2 \int d\nu \mathbf{F}_\nu^j$ , satisfies

$\nabla \cdot \mathbf{F} = 0$ , so that

$$\nabla \cdot \mathbf{F} = 2\rho \sum_{j=1}^2 \int d\nu \int_+ d\mathbf{k} \kappa_j^{\text{abs}}(\mathbf{k}) \left[ \frac{B_\nu}{2} - i_\nu^j(\mathbf{k}) \right] = 0. \quad (2.13)$$

Also, for an atmosphere with an effective temperature  $T_{\text{eff}}$ , the total flux is constant and satisfies

$$F_z = \sum_{j=1}^2 \int d\nu \int d\mathbf{k} \mu I_\nu^j(\mathbf{k}) = 2 \sum_{j=1}^2 \int d\nu \int_+ d\mathbf{k} \mu f_\nu^j(\mathbf{k}) = \sigma_{\text{SB}} T_{\text{eff}}^4, \quad (2.14)$$

where  $\sigma_{\text{SB}}$  is the Stefan–Boltzmann constant.

## 2.2 Special case: magnetic field parallel to surface normal

In the special case when  $\mathbf{B}$  is parallel to the surface normal  $\hat{\mathbf{z}}$ , the intensity  $I_\nu^j(\mathbf{k})$  is independent of  $\phi$ , so that  $I_\nu^j(\mathbf{k}) = I_\nu^j(\mu)$ . In the atmosphere models based on the full RTE presented in this paper, we consider only this special case. It is clear that the RTE (2.8) can be written in the familiar form

$$\mu^2 \frac{\partial i_\nu^j}{\partial \tau_\nu} = i_\nu^j - S_\nu^j, \quad (2.15)$$

where

$$S_\nu^j(\mu) = \frac{\kappa_j^{\text{abs}}(\mu) B_\nu}{\kappa_j^{\text{tot}}(\mu)} \frac{1}{2} + \frac{4\pi}{\kappa_j^{\text{tot}}(\mu)} \sum_{i=1}^2 \int_0^1 d\mu' \frac{d\kappa^{\text{sc}}(\mu' i \rightarrow \mu j)}{d\Omega} i_\nu^i(\mu') \quad (2.16)$$

is the source function.

We note that, in using equation (2.16) to calculate the source function, the integral over the initial photon direction  $\mu'$  must be carried out at every frequency  $\nu$ , depth  $\tau$ , and final photon direction  $\mu$  and for each global iteration (temperature correction) as described in Section 3. We can reduce the computation time by assuming that the differential scattering cross-section is approximately independent of the initial photon direction. Equation (2.16) then yields the approximate source function

$$S_\nu^j(\mu) \approx \frac{\kappa_j^{\text{abs}}(\mu) B_\nu}{\kappa_j^{\text{tot}}(\mu)} \frac{1}{2} + \sum_{i=1}^2 \frac{\kappa_{ji}^{\text{sc}}(\mu) c u_\nu^i}{\kappa_j^{\text{tot}}(\mu) 4\pi}, \quad (2.17)$$

where the specific energy density is

$$u_\nu^j = \frac{1}{c} \int d\mathbf{k} I_\nu^j(\mathbf{k}). \quad (2.18)$$

We expect that this approximation introduces only a small error to the emergent spectra, and a comparison of the final results using the source functions given by equations (2.16) and (2.17) indeed shows the differences are small, though this has not been studied extensively (see also Shibano & Zavlin 1995). The numerical results presented in Section 4 make use of the approximate source function given by equation (2.17).

## 2.3 Diffusion approximation

In this paper, we shall also present atmosphere models for general  $\Theta_B$  based on the diffusion approximation of the RTE. To obtain the diffusion RTE, we multiply both sides of the RTE (2.1) by  $-k/\rho\kappa_j^{\text{tot}}(\mathbf{k})$  and integrate over the solid angle to find the specific

flux,

$$\mathbf{F}_\nu^j = - \int d\mathbf{k} \frac{1}{\rho\kappa_j^{\text{tot}}(\mathbf{k})} \mathbf{k} (\mathbf{k} \cdot \nabla) I_\nu^j(\mathbf{k}), \quad (2.19)$$

where we have used the symmetry property of the opacities, so that  $\int d\mathbf{k} [\mathbf{k}/\kappa_j^{\text{tot}}(\mathbf{k})] [d\kappa^{\text{sc}}(\mathbf{k}' i \rightarrow \mathbf{k} j)/d\Omega] = 0$  and  $\int d\mathbf{k} \mathbf{k} [\kappa_j^{\text{abs}}(\mathbf{k})/\kappa_j^{\text{tot}}(\mathbf{k})] = 0$ . In the diffusion limit, we approximate the specific intensity by  $I_\nu^j(\mathbf{k}) \approx (c/4\pi)[u_\nu^j + (3/c)\mathbf{k} \cdot \mathbf{F}_\nu^j]$ . Substituting into equation (2.19) and using the fact that  $\nabla u_\nu^j = (\partial u_\nu^j/\partial z)\hat{\mathbf{z}}$  and that the opacity only depends on  $\mu_B = \mathbf{k} \cdot \hat{\mathbf{B}} = \cos \theta_B$ , we find

$$\mathbf{F}_\nu^j \approx -c \frac{\partial u_\nu^j}{\partial z} (l_j^\parallel \cos \Theta_B \hat{\mathbf{B}} + l_j^\perp \sin \Theta_B \hat{\mathbf{B}}_\perp), \quad (2.20)$$

where  $\hat{\mathbf{B}}_\perp$  is the unit vector perpendicular to  $\hat{\mathbf{B}}$  and lies in the plane of  $\hat{\mathbf{B}}$  and  $\hat{\mathbf{z}}$  (recall that  $\Theta_B$  is the angle between  $\hat{\mathbf{B}}$  and  $\hat{\mathbf{z}}$ ) and  $\hat{\mathbf{B}}_\perp \sin \Theta_B = \hat{\mathbf{z}} - (\hat{\mathbf{z}} \cdot \hat{\mathbf{B}})\hat{\mathbf{B}}$ . In equation (2.20),  $l_j^\parallel$  and  $l_j^\perp$  are the angle-averaged mean free paths parallel and perpendicular to the magnetic field, respectively, and they are given by:

$$l_j^\parallel = \int_0^1 d\mu_B \frac{\mu_B^2}{\rho\kappa_j^{\text{tot}}(\mu_B)}, \quad (2.21)$$

$$l_j^\perp = \frac{1}{2} \int_0^1 d\mu_B \frac{(1 - \mu_B^2)}{\rho\kappa_j^{\text{tot}}(\mu_B)}. \quad (2.22)$$

The specific flux perpendicular to the stellar surface is  $F_{\nu,z}^j \approx -cl_j(\partial u_\nu^j/\partial z)$ , where the averaged mean free path along  $z$  is

$$l_j = l_j^\parallel \cos^2 \Theta_B + l_j^\perp \sin^2 \Theta_B. \quad (2.23)$$

Note that, as a consequence of equation (2.20), a magnetic field can induce horizontal radiative flux; this implies that a horizontal temperature gradient may develop in the atmosphere. To address this issue properly, one needs to study the three-dimensional structure of the atmosphere; this is beyond the scope of this paper (see Section 5). Substituting the approximate expressions of the specific intensity and flux into the zeroth-order moment equation (2.11) and defining the Thomson depth  $d\tau = -\rho\kappa_0^{\text{es}} dz$  and the zero-field Thomson mean free path  $l_0 \equiv 1/(\rho\kappa_0^{\text{es}})$ , we obtain

$$\frac{\partial}{\partial \tau} \left( \frac{l_j}{l_0} \frac{\partial u_\nu^j}{\partial \tau} \right) = \frac{K_j^{\text{abs}}}{\kappa_0^{\text{es}}} \left( u_\nu^j - \frac{u_\nu^{\text{P}}}{2} \right) + \frac{K_{21}^{\text{sc}}}{\kappa_0^{\text{es}}} (u_\nu^j - u_\nu^{3-j}), \quad (2.24)$$

where  $u_\nu^{\text{P}} = (4\pi/c)B_\nu(T)$  is the blackbody specific energy density and

$$K_j^{\text{abs}} = \frac{1}{4\pi} \int d\mathbf{k} \kappa_j^{\text{abs}}(\mathbf{k}), \quad (2.25)$$

$$K_j^{\text{tot}} = \frac{1}{4\pi} \int d\mathbf{k} \kappa_j^{\text{tot}}(\mathbf{k}), \quad (2.26)$$

$$K_{ji}^{\text{sc}} = \frac{1}{4\pi} \int d\mathbf{k} \kappa_{ji}^{\text{sc}}(\mathbf{k}). \quad (2.27)$$

This equation has been previously derived by Kaminker, Pavlov & Shibano (1982, 1983).

The boundary conditions for equation (2.24) are  $\hat{\mathbf{z}} \cdot \mathbf{F}_\nu^j = cu_\nu^j/2$  at  $\tau = 0$  and  $u_\nu^j \rightarrow u_\nu^{\text{P}}/2$  at  $\tau \rightarrow \infty$ , i.e.,

$$\frac{l_j}{l_0} \frac{\partial u_\nu^j}{\partial \tau} = \frac{u_\nu^j}{2} \quad \text{at } \tau = 0 \quad (2.28)$$

$$\frac{\partial u_\nu^j}{\partial \tau} + u_\nu^j = \frac{1}{2} \left( \frac{\partial u_\nu^{\text{P}}}{\partial \tau} + u_\nu^{\text{P}} \right) \quad \text{at } \tau \rightarrow \infty. \quad (2.29)$$



Finally, in the diffusion approximation, the radiative equilibrium condition (see equation 2.13) simplifies to

$$\frac{dF_z}{d\tau} = c \sum_{j=1}^2 \int d\nu \frac{K_j^{\text{abs}}}{\kappa_0^{\text{cs}}} \left( u_\nu^j - \frac{u_\nu^{\text{P}}}{2} \right) = 0. \quad (2.30)$$

## 2.4 Hydrostatic equilibrium and equation of state

In modelling the atmosphere, we must determine the density  $\rho(\tau)$  and temperature  $T(\tau)$  along with the radiation intensity. From hydrostatic equilibrium, the pressure  $P$  at Thomson depth  $\tau$  is given by

$$P(\tau) = \frac{g}{\kappa_0^{\text{cs}}} \tau, \quad (2.31)$$

where  $g = (GM/R^2)(1 - 2GM/Rc^2)^{-1/2} = 2.4 \times 10^{14} \text{ cm s}^{-2}$  is the gravitational acceleration at the surface of a  $M = 1.4 M_\odot$ ,  $R = 10 \text{ km}$  NS. We assume the atmosphere is fully ionized. The equation of state can be written as

$$P = P_e + P_{\text{ion}} + P_{\text{Coul}}, \quad (2.32)$$

where  $P_e$  is the pressure due to electrons, which may or may not be degenerate,  $P_{\text{ion}}$  is the pressure due to ions, which still behave as a classical ideal gas under the conditions that exist in the upper layers of the NS, and  $P_{\text{Coul}}$  is the Coulomb correction to the pressure. In strong magnetic fields, electrons are quantized into Landau levels, and the electron pressure is given by (e.g. Lai 2001)

$$P_e = \frac{m_e c^2}{2^{1/2} \pi^2 \lambda_e^3 B_Q} \left( \frac{kT}{m_e c^2} \right)^{3/2} \sum_{\nu=0}^{\infty} g_\nu F_{1/2} \left( \frac{\mu_e - \nu \hbar \omega_{Be}}{kT} \right), \quad (2.33)$$

where  $\lambda_e = \hbar/m_e c$  is the electron Compton wavelength,  $B_Q = m_e^2 c^3/(e \hbar) = 4.414 \times 10^{13} \text{ G}$ ,  $g_\nu$  is the spin degeneracy of the Landau level ( $g_0 = 1$  and  $g_\nu = 2$  for  $\nu \geq 1$ ),  $\mu_e$  is the electron chemical potential, and  $F_n(y)$  is the Fermi–Dirac integral

$$F_n(y) \equiv \int_0^\infty \frac{x^n}{e^{x-y} + 1} dx. \quad (2.34)$$

When the conditions

$$T \ll T_B = \frac{\hbar \omega_{Be}}{k} = 1.34 \times 10^8 B_{12} \text{ K} \quad (2.35)$$

$$\rho \leq \rho_B = \frac{m_p}{\sqrt{2} \pi^2 Y_e R_Q^3} = 7.05 \times 10^3 Y_e^{-1} B_{12}^{3/2} \text{ g cm}^{-3}, \quad (2.36)$$

where  $R_Q = (\hbar c/eB)^{1/2}$  and  $B_{12} = B/(10^{12} \text{ G})$ , are satisfied, as in the case of the atmospheres considered in this paper, only the ground Landau level ( $\nu = 0$ ) is occupied. Thus, in equation (2.33), only the first term in the sum need be considered. The electron number density  $n_e$  is given by

$$n_e = \frac{1}{2^{3/2} \pi^2 \lambda_e^3 B_Q} \left( \frac{kT}{m_e c^2} \right)^{1/2} F_{-1/2} \left( \frac{\mu_e}{kT} \right), \quad (2.37)$$

where we have kept only the  $\nu = 0$  term. For  $\rho \leq \rho_B$ , the electron Fermi temperature is

$$T_F = E_F/k = 2.70 B_{12}^{-2} (Y_e \rho_1)^2 \text{ K}, \quad (\text{for } \rho \leq \rho_B) \quad (2.38)$$

where  $\rho_1 = \rho/(1 \text{ g cm}^{-3})$ . Because electrons are confined by the

magnetic fields to smaller volumes, electron degeneracy occurs at higher densities than in the absence of the magnetic field. Note that for  $T \gg T_F$ , equation (2.33) reduces to  $P_e \approx n_e kT$  even when the field is strongly quantizing ( $\rho \leq \rho_B$ ). The ion pressure, on the other hand, is well approximated by

$$P_{\text{ion}} = \frac{\rho kT}{Am_p}. \quad (2.39)$$

The Coulomb correction is given by (e.g. Shapiro & Teukolsky 1983)

$$P_{\text{Coul}} = -\frac{3}{10} \left( \frac{4\pi}{3} \right)^{1/3} Z^{2/3} e^2 n_e^{4/3}. \quad (2.40)$$

The equation of state, including the effects of degeneracy, is determined by substituting the different components of the pressure into equation (2.32) to obtain a relation between a given total pressure  $P(\tau)$  and temperature  $T(\tau)$ . The root of this equation yields the degeneracy parameter  $\eta(\tau) = \mu_e/(kT)$  which is then substituted into equation (2.37) to obtain the electron number density  $n_e$  and the total density  $\rho = (Am_p/Z)n_e$ . We use the rational function approximation given by Antia (1993) to evaluate the Fermi–Dirac integrals. For all the non-magnetic and magnetic atmosphere models considered here, the difference between the densities calculated from the ideal gas equation of state and the equation of state including electron degeneracy is only a few per cent in the innermost layers, and the effect on the surface spectrum is negligible (see Section 4).

## 2.5 Opacities

In a magnetized electron–ion plasma, the scattering and free–free absorption opacities depend on the direction of propagation  $\mathbf{k}$  (more precisely, on the angle  $\theta_B$  between  $\mathbf{k}$  and  $\hat{\mathbf{B}}$ ) and the normal modes ( $j = 1, 2$ ) of the electromagnetic waves. In rotating coordinates, with the  $z$ -axis along  $\hat{\mathbf{B}}$ , the components of the polarization vector  $\mathbf{e}^j$  are given by (see Appendix A)

$$|e_\pm^j|^2 = \left| \frac{1}{\sqrt{2}} (e_x^j \pm i e_y^j) \right|^2 = \frac{1}{2(1 + K_j^2 + K_{zj}^2)} [1 \pm (K_j \cos \theta_B + K_{zj} \sin \theta_B)]^2 \quad (2.41)$$

$$|e_z^j|^2 = \frac{1}{1 + K_j^2 + K_{zj}^2} (K_j \sin \theta_B - K_{zj} \cos \theta_B)^2, \quad (2.42)$$

where

$$K_j = \beta \left[ 1 + (-1)^j \left( 1 + \frac{1}{\beta^2} \right)^{1/2} \right], \quad (2.43)$$

$$K_{zj} = \frac{u_e v (1 - u_i - M^{-1}) \sin \theta_B \cos \theta_B K_j - u_e^{1/2} v \sin \theta_B}{(1 - u_e)(1 - u_i) - v[(1 - u_i)(1 - u_e \cos^2 \theta_B) - M u_i \sin^2 \theta_B]}, \quad (2.44)$$

$$\beta = \frac{u_e^{1/2}}{2(1 - v) \cos \theta_B} \left( 1 - u_i - \frac{1 + v}{M} \right), \quad (2.45)$$

and  $M \equiv Am_p/(Zm_e)$ . In equations (2.43)–(2.45), we have defined

$$u_e = \frac{\omega_{Be}^2}{\omega^2}, \quad u_i = \frac{\omega_{Bi}^2}{\omega^2}, \quad v = \frac{\omega_p^2}{\omega^2}; \quad (2.46)$$

the electron cyclotron frequency  $\omega_{Be}$ , the ion cyclotron frequency

$\omega_{Bi}$ , and the electron plasma frequency  $\omega_p$  are given by

$$\hbar\omega_{Be} = \frac{\hbar eB}{m_e c} = 11.58 B_{12} \text{ keV}, \quad (2.47)$$

$$\hbar\omega_{Bi} = \hbar \frac{ZeB}{Am_p c} = 6.305 B_{12} \left(\frac{Z}{A}\right) \text{ eV}, \quad (2.48)$$

and

$$\hbar\omega_p = \hbar \left( \frac{4\pi e^2 n_e}{m_e} \right)^{1/2} = 28.71 \left(\frac{Z}{A}\right)^{1/2} \rho_1^{1/2} \text{ eV}, \quad (2.49)$$

respectively. Note that in the coordinate frame where the  $z$ -axis is along  $\mathbf{k}$  and the  $x$ -axis is in the  $\mathbf{k}$ - $\mathbf{B}$  plane, the polarization vector can be written as (see Appendix A)

$$\mathbf{e}^j = \frac{1}{\sqrt{1 + K_j^2 + K_{zj}^2}} (iK_j, 1, iK_{zj}). \quad (2.50)$$

Thus the modes are elliptically polarized with  $K_j$  being the ratio of the axes of the ellipse. It is easy to show that  $K_1 = -K_2^{-1}$  and  $|K_1| < 1$ ; this implies that the extraordinary mode ( $j = 1$ ) is mostly perpendicular to the  $\mathbf{k}$ - $\mathbf{B}$  plane, while the ordinary mode ( $j = 2$ ) lies mainly in the  $\mathbf{k}$ - $\mathbf{B}$  plane. For  $\omega \ll \omega_{Be}$ , the modes are nearly linearly polarized at most angles except close to parallel propagation  $\theta_B = 0$  and  $\pi$ , where the polarization is circular since  $K_j = (-1)^j$ . In this limit,  $|e_\pm^j|^2$  and  $|e_z^j|^2 \sim 1$ , and  $|e_z^1|^2 \sim \beta^{-2}$  [see Section 2.6, specifically equations (2.64) and (2.65)].

It is evident from equation (2.44) that the component of  $\mathbf{e}^j$  along  $\mathbf{k}$  is of order  $v \propto \rho/\omega^2$ , and thus, at sufficiently low densities,  $K_{zj}$  can be neglected so that the modes are transverse. Previous studies adopted this ‘transverse-mode’ approximation when treating the radiative opacities in a magnetized medium (e.g. Pavlov et al. 1995). As we shall see in Section 4, since the radiation can directly emerge from deep layers where  $v \gtrsim 1$ , the transverse-mode approximation cannot always be justified.

In a magnetized medium, the electron scattering opacity from mode  $j$  into mode  $i$  is given by (Ventura 1979; Ventura, Nagel & Mészáros 1979)

$$\kappa_{ji}^{es} = \frac{n_e \sigma_T}{\rho} \sum_{\alpha=-1}^1 \frac{\omega^2}{(\omega + \alpha\omega_{Be})^2 + \nu_e^2} |e_\alpha^j|^2 A_\alpha^i, \quad (2.51)$$

where  $A_\alpha^i$  is the angle integral given by

$$A_\alpha^i = \frac{3}{8\pi} \int d\mathbf{k} |e_\alpha^i|^2. \quad (2.52)$$

The electron scattering opacity from mode  $j$  is

$$\kappa_j^{es} = \frac{n_e \sigma_T}{\rho} \sum_{\alpha=-1}^1 \frac{\omega^2}{(\omega + \alpha\omega_{Be})^2 + \nu_e^2} |e_\alpha^j|^2 A_\alpha, \quad (2.53)$$

where  $A_\alpha = \sum_{i=1}^2 A_\alpha^i$ . In the transverse-mode approximation ( $K_{zj} = 0$ ), the polarization vector  $\mathbf{e}^j$  satisfies the completeness relation  $\sum_{j=1}^2 |e_\pm^j|^2 = (1 + \cos^2 \theta_B)/2$  and  $\sum_{j=1}^2 |e_z^j|^2 = \sin^2 \theta_B$ , and thus  $A_\alpha = 1$ . Note that a resonance develops near the electron cyclotron frequency for the circularly polarized mode with its electric field rotating in the same direction as the electron gyration; however, this resonance appears only in the extraordinary mode since one can easily show that  $|e_z^j|^2 \approx 0$  at  $\omega = \omega_{Be}$ . For the photon energies of interest in this paper, i.e.  $\omega \ll \omega_{Be}$ , a suppression factor  $(\omega/\omega_{Be})^2$  in the opacity results from the strong confinement of electrons perpendicular to the magnetic field.

Similar features appear in the electron free-free absorption opacity (e.g. Virtamo & Jauho 1975; Pavlov & Panov 1976; Nagel & Ventura 1983)

$$\kappa_j^{\text{ff},e} = \frac{\alpha_0}{\rho} \sum_{\alpha=-1}^1 \frac{\omega^2}{(\omega + \alpha\omega_{Be})^2 + \nu_e^2} |e_\alpha^j|^2 \bar{g}_\alpha^{\text{ff}}, \quad (2.54)$$

where

$$\begin{aligned} \alpha_0 &= 4\pi^2 Z^2 \alpha_F^3 \frac{\hbar^2 c^2}{m_e^2} \left( \frac{2m_e}{\pi kT} \right)^{1/2} \frac{n_e n_i}{\omega^3} (1 - e^{-\hbar\omega/kT}) \\ &= \alpha_0^{\text{ff}} \frac{3\sqrt{3}}{4\pi} \frac{1}{\bar{g}^{\text{ff}}}, \end{aligned} \quad (2.55)$$

$\alpha_F = e^2/(\hbar c)$  is the fine structure constant, and  $\alpha_0^{\text{ff}}$  and  $\bar{g}^{\text{ff}}$  are the free-free absorption coefficient and velocity-averaged free-free Gaunt factor, respectively, in the absence of a magnetic field. In equation (2.54),  $\bar{g}_{\pm 1}^{\text{ff}} = \bar{g}_\pm^{\text{ff}}$  and  $\bar{g}_0^{\text{ff}} = \bar{g}_\parallel^{\text{ff}}$  are the velocity-averaged free-free Gaunt factors in a magnetic field, which we evaluate using the expressions given by Mészáros (1992) (see also Nagel 1980; note these expressions for the Gaunt factors neglect transitions to the excited electron Landau levels; see Pavlov & Panov 1976 for the complete expressions).

In an ionized medium, the ions also contribute to the total scattering and absorption opacities. Analogous to equations (2.51)–(2.54), we have

$$\kappa_{ji}^{is} = \left( \frac{Z^2 m_e}{Am_p} \right)^2 \frac{n_i \sigma_T}{\rho} \sum_{\alpha=-1}^1 \frac{\omega^2}{(\omega - \alpha\omega_{Bi})^2 + \nu_i^2} |e_\alpha^j|^2 A_\alpha^i, \quad (2.56)$$

$$\kappa_j^{is} = \left( \frac{Z^2 m_e}{Am_p} \right)^2 \frac{n_i \sigma_T}{\rho} \sum_{\alpha=-1}^1 \frac{\omega^2}{(\omega - \alpha\omega_{Bi})^2 + \nu_i^2} |e_\alpha^j|^2 A_\alpha, \quad (2.57)$$

and

$$\kappa_j^{\text{ff},i} = \frac{1}{Z^3} \left( \frac{Z^2 m_e}{Am_p} \right)^2 \frac{\alpha_0}{\rho} \sum_{\alpha=-1}^1 \frac{\omega^2}{(\omega - \alpha\omega_{Bi})^2 + \nu_i^2} |e_\alpha^j|^2 \bar{g}_\alpha^{\text{ff},i}. \quad (2.58)$$

Note that the ion cyclotron resonance occurs for  $\alpha = +1$ , i.e., when the electric field of the mode rotates in the same direction as the ion gyration. The total scattering and absorption opacities in a fully ionized medium is then the sum of the electron and ion components, namely  $\kappa_j^{\text{sc}} = \kappa_j^{\text{es}} + \kappa_j^{\text{is}}$  and  $\kappa_j^{\text{abs}} = \kappa_j^{\text{ff},e} + \kappa_j^{\text{ff},i}$ .

In equations (2.51)–(2.58), we have included damping through  $\nu_e = \nu_{r,e} + \nu_{c,e}$  and  $\nu_i = \nu_{r,i} + \nu_{c,i}$ , where  $\nu_{r,e} = (2e^2/3m_e c^3)\omega^2$  and  $\nu_{r,i} = (Z^2 m_e/Am_p)\nu_{r,e}$  are radiative damping rates and  $\nu_{c,e} = (\alpha_0 \bar{g}_\alpha^{\text{ff}}/n_e \sigma_T)\nu_{r,e}$  and  $\nu_{c,i} = (m_e/Am_p)\nu_{c,e}$  are collisional damping rates (see Pavlov et al. 1995 and references therein). Note that the natural width of the ion cyclotron resonance is determined by the dimensionless damping rate  $\gamma_i \equiv \nu_i/\omega = \gamma_{r,i} + \gamma_{\alpha,i}$ , with radiative and collisional contributions given by

$$\gamma_{r,i} = 5.18 \times 10^{-9} \frac{Z^2}{A} \left( \frac{\hbar\omega}{\text{keV}} \right) \quad (2.59)$$

and

$$\begin{aligned} \gamma_{\alpha,i} &= 8.42 \times 10^{-8} \frac{Z^2}{A} \bar{g}_\alpha^{\text{ff}} (1 - e^{-\hbar\omega/kT}) \\ &\times \left( \frac{10^6 \text{ K}}{T} \right)^{1/2} \left( \frac{n_i}{10^{24} \text{ cm}^{-3}} \right) \left( \frac{\text{keV}}{\hbar\omega} \right)^2. \end{aligned} \quad (2.60)$$

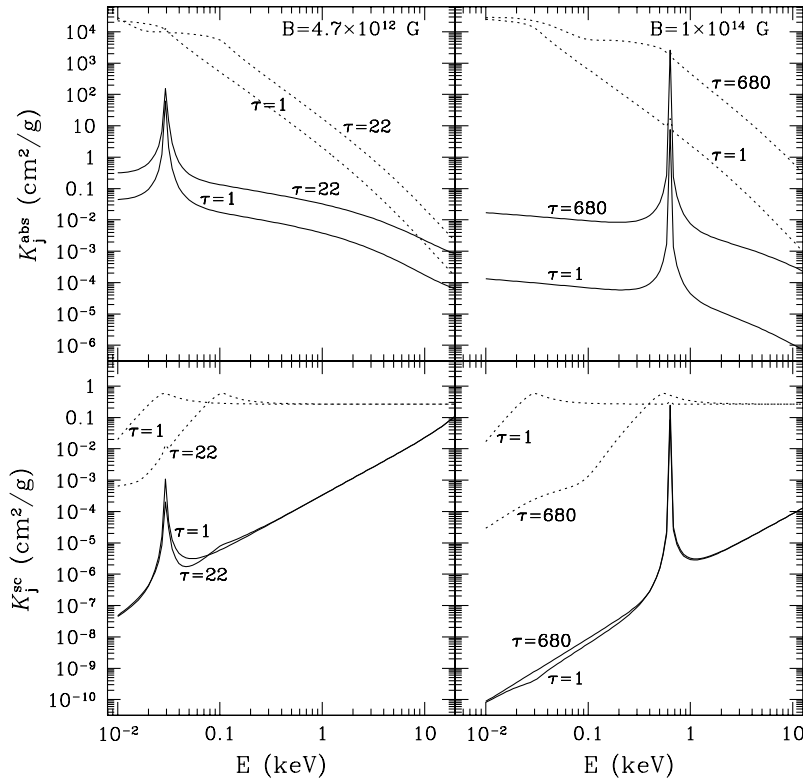


**Figure 1.** Angle-averaged absorption opacities  $K_j^{\text{abs}}$  (upper panels) and scattering opacities  $K_j^{\text{sc}}$  (lower panels) as functions of energy for magnetic fields  $B = 4.7 \times 10^{12}$  (left panels) and  $10^{14}$  G (right panels). The densities and temperatures are chosen to be representative of the H atmospheres ( $Z = A = 1$ ) studied in Section 4 (see Fig. 5): for  $B = 4.7 \times 10^{12}$  G, Thomson depth  $\tau = 1$  corresponds to  $\rho = 1 \text{ g cm}^{-3}$  and  $T = 3.7 \times 10^6$  K and  $\tau = 22$  corresponds to  $\rho = 13 \text{ g cm}^{-3}$  and  $T = 5.9 \times 10^6$  K; for  $B = 10^{14}$  G, Thomson depth  $\tau = 1$  corresponds to  $\rho = 1.1 \text{ g cm}^{-3}$  and  $T = 3.4 \times 10^6$  K and  $\tau = 680$  corresponds to  $\rho = 370 \text{ g cm}^{-3}$  and  $T = 7.0 \times 10^6$  K. The solid lines are for the extraordinary mode ( $j = 1$ ) and the dotted lines are for the ordinary mode ( $j = 2$ ). We note that the non-magnetic opacities are similar to the ordinary mode opacities in terms of energy dependence, and the variations in the ordinary mode opacities at low energies ( $E \lesssim \hbar\omega_p$ ) are because of  $K_{zj} \propto \omega_p^2$ ; see equation (2.44)].

Also, the thermal width of the ion cyclotron linewidth is of order

$$\gamma_{\text{th}} = \left( \frac{2kT}{Am_p c^2} \right)^{1/2} = 1.46 \times 10^{-3} A^{-1/2} \left( \frac{T}{\text{keV}} \right)^{1/2}; \quad (2.61)$$

the Doppler broadening would presumably change the line profile from the Lorentzian to the Voigt profile (e.g. Mihalas 1978). Since  $\gamma_{r,i}, \gamma_{a,i}, \gamma_{\text{th}} \ll 1$ , damping is negligible except very near resonance (see Section 2.6).

## 2.6 Behaviour of opacities and ion cyclotron resonance

Fig. 1 shows the angle-averaged absorption opacity  $K_j^{\text{abs}}$  and scattering opacity  $K_j^{\text{sc}} = \sum_{i=1}^2 K_{ji}^{\text{sc}}$  [see equations (2.25)–(2.27)] as functions of energy for magnetic fields  $B = 4.7 \times 10^{12}$  and  $10^{14}$  G at densities and temperatures characteristic of NS atmospheres. For angles  $\theta_B$  not too close to  $0^\circ$  or  $180^\circ$  (e.g.,  $10^\circ \lesssim \theta_B \lesssim 170^\circ$ ), the unaveraged opacities  $\kappa_j^{\text{sc}}$  and  $\kappa_j^{\text{abs}}$  resemble  $K_j^{\text{sc}}$  and  $K_j^{\text{abs}}$  in qualitative behaviour, while exhibiting strong angle dependence on  $\theta_B$  near  $0^\circ$  or  $180^\circ$ . The most prominent feature in Fig. 1 is the ion cyclotron resonance at  $\hbar\omega_{Bi} = 0.63 B_{14} \text{ keV}$  (for  $Z = A = 1$ ), where  $B_{14} = B/(10^{14} \text{ G})$ , for the extraordinary mode. Note that the cyclotron feature does not possess the usual Voigt profile that characterizes spectral lines; the feature is rather broad with  $\Delta E/E \sim 1 + 10^{-3} B_{14}^{-2} \rho_1$  [see equations (2.69)–(2.70) below], which is far wider than the natural or thermal width [see equations (2.59)–(2.61)]. Away from the resonance, the extraordinary-mode

opacities are suppressed relative to the zero-field values by a factor  $(\omega/\omega_{Be})^2$  (see below). For the ordinary mode, the opacities are similar to the non-magnetic values (see below) except at high densities/low frequencies, i.e.  $v \gtrsim 1$ , where the effects of  $K_{zj}$  become important (see equation 2.44).

The behaviour of the opacities, especially the ion cyclotron feature, shown in Fig. 1 can be understood as follows. For the magnetic field strength and photon energy of interest in this paper,  $\hbar\omega \ll \hbar\omega_{Be} = 11.6 B_{12} \text{ keV}$ , the scattering and free–free absorption opacities can be written as

$$\kappa_j^{\text{sc}} = \frac{n_e \sigma_T}{\rho} \xi_j^i, \quad \kappa_j^{\text{abs}} = \frac{\alpha_0}{\rho} \xi_j^i, \quad (2.62)$$

with

$$\xi_j^i \approx \left( \frac{1}{u_e} |e_+^j|^2 + \frac{1}{u_e} |e_-^j|^2 + |e_z^j|^2 \right) + \frac{1}{M'^2} \left[ \frac{1}{(1 - \sqrt{u_i})^2 + \gamma_i^2} |e_+^j|^2 + \frac{1}{(1 + \sqrt{u_i})^2} |e_-^j|^2 + |e_z^j|^2 \right], \quad (2.63)$$

where  $M' = (Am_p/Zm_e)Z^{-1/2}$  for scattering and  $M' = (Am_p/Zm_e)Z^{1/2}$  for absorption, and we have set the free–free Gaunt factors to unity in  $\kappa_j^{\text{abs}}$  and  $A_\alpha = 1$  in  $\kappa_j^{\text{sc}}$  for simplicity. In the following, we shall consider photon energies such that  $|u_i - 1| \gtrsim \gamma_i, \gamma_{\text{th}}$  [see equations (2.59)–(2.61)], and we shall drop

the  $\gamma_i^2$  term from equation (2.63). Also for simplicity, we shall set  $Z = A = 1$ .

For  $\theta_B$  not too small, i.e.  $\sin^2 \theta_B / \cos \theta_B \sim 1$ , the polarization parameter  $\beta$  (see equation 2.45) satisfies  $|\beta| \gg 1$  except when  $\omega$  is very close to the ion cyclotron resonance (i.e.  $|1 - u_i - (1 + v)/M| \lesssim u_e^{-1/2}$ ) or when  $\hbar\omega \lesssim \hbar\omega_p^2 / \omega_{Be} = 0.07 \rho_1 B_{12}^{-1}$  eV. In the limit of  $|\beta| \gg 1$ , we find  $K_1 = -1/(2\beta)$  and  $K_2 = 2\beta$ , and thus

$$|e_{\pm}^1|^2 = \frac{1}{2} \left( 1 \mp \frac{1}{\beta} \cos \theta_B \right), \quad |e_{\pm}^1|^2 = \frac{1}{(2\beta)^2} \sin^2 \theta_B, \quad (2.64)$$

$$|e_{\pm}^2|^2 = \frac{1}{2} \cos^2 \theta_B \left( 1 \pm \frac{1}{\beta \cos \theta_B} \right),$$

$$|e_{\pm}^2|^2 = \left[ 1 - \frac{1}{(2\beta)^2} \right] \sin^2 \theta_B, \quad (2.65)$$

where, for simplicity, we have taken the transverse approximation so that  $K_{z,j} \approx 0$ . Substituting these into equation (2.63), we obtain, for  $|\beta| \gg 1$ ,

$$\xi^1 \approx \frac{1}{u_e} \left[ 1 + \frac{(1-v)^2 \cos^2 \theta_B / \sin^2 \theta_B + u_i(1+u_i)}{(1-u_i)^2} \right], \quad (2.66)$$

and

$$\xi^2 \approx \sin^2 \theta_B + \frac{1}{u_e}$$

$$\times \left[ (\cos^2 \theta_B + u_i \sin^2 \theta_B) + \cos^2 \theta_B \frac{u_i(1+u_i) - (1-v)^2 / \sin^2 \theta_B}{(1-u_i)^2} \right]. \quad (2.67)$$

Clearly, away from ion cyclotron resonance,  $\xi^1 \propto u_e^{-1} = (\omega / \omega_{Be})^2$ , and thus the opacities for the extraordinary mode are suppressed compared to the zero-field values:

$$\kappa_1^{\text{sc}} \propto \left( \frac{\omega}{\omega_{Be}} \right)^2, \quad \kappa_1^{\text{abs}} \propto \frac{1}{\omega_{Be}^2 \omega} (1 - e^{-\hbar\omega/kT}). \quad (2.68)$$

At high densities/low frequencies, such that  $v \gtrsim 1$ , these are multiplied by a term of order  $1 + O(v^2)$ ; for  $v \gg 1$ , we have  $\kappa_1^{\text{sc}} \propto \omega_p^4 / (\omega_{Be}^2 \omega^2)$ . For the ordinary mode,  $\xi^2 \sim 1$ , and thus the opacities are approximately unchanged from the zero-field values.

Equations (2.66) and (2.67) also apply to photon energies near the ion cyclotron resonance as long as  $|1 - u_i| \gg (1 + v)/M$ , so that  $|\beta| \gg 1$  (note that we are considering typical angles where  $|\cos \theta_B| \sim 1$ ). It is evident from equation (2.66) that, for the extraordinary mode, the opacities exhibit a broad peak/feature around  $\omega_{Bi}$ , i.e. the term contained inside the brackets in equation (2.66) becomes significantly greater than unity. The width of the feature,  $|1 - u_i|$ , is of order

$$\Gamma_i \equiv \left| \frac{\omega - \omega_{Bi}}{\omega_{Bi}} \right| \approx \left[ 2 + (1 - v^{\text{res}})^2 \frac{\cos^2 \theta_B}{\sin^2 \theta_B} \right]^{1/2}, \quad (2.69)$$

where

$$v^{\text{res}} = \frac{\omega_p^2}{\omega_{Bi}^2} \approx \left( \frac{\rho}{1 \text{ g cm}^{-3}} \right) \left( \frac{B}{4.6 \times 10^{12} \text{ G}} \right)^{-2}. \quad (2.70)$$

It is important to note that, although the natural and thermal width of the ion cyclotron line are rather narrow [see equations (2.59)–(2.61)], the cyclotron feature as described by equations (2.66) and (2.69) is broad, i.e., the opacities are significantly affected by the ion cyclotron resonance for  $0.3 \lesssim \omega / \omega_{Bi} \lesssim 3$ . Also, equation

(2.67) indicates that, although the ion cyclotron resonance formally occurs for the ordinary mode, its strength is diminished by the  $(\omega / \omega_{Be})^2 = (m_e / m_p)^2$  suppression.

Finally, we note that the presence of ions induces a mode-collapse point very near  $\omega_{Bi}$ . This can be seen from equation (2.45), which shows that  $\beta = 0$  when  $1 - u_i - (1 + v)/M = 0$  or  $\omega = \omega_{Bi}[1 + (1 + v)/2M]$ . At this point, the two photon modes become degenerate (both are circularly polarized), and the transport equation (2.1) formally breaks down. This ion-induced mode collapse is independent of the well-known mode collapse as a result of vacuum polarization (Pavlov & Shibano 1979; Ventura et al. 1979; see Section 5). Note, however, that the ion-induced mode-collapse feature is very narrow [ $|\beta| \ll 1$  requires  $|1 - u_i - (1 + v)/M| \ll u_e^{-1/2}$ ], so it is completely ‘buried’ by the much wider and more prominent ion cyclotron feature.

### 3 NUMERICAL METHOD

#### 3.1 Magnetic atmospheres with full radiative transport

When presenting results of atmosphere models based on the full transport equations, we consider only the case of  $\mathbf{B}$  perpendicular to the surface ( $\Theta_B = 0^\circ$ ). Thus the radiation intensity  $I_\nu^j$  depends on depth  $\tau$ , energy  $E = \hbar\omega = h\nu$ , and angle  $\theta$ .

We construct a grid in Thomson depth, energy, and angle with intervals that are equally spaced logarithmically from  $10^{-4}$  to  $\sim 10^3$  in depth and from  $10^{-2}$  to  $\sim 10$  keV in energy and spaced every  $5^\circ$  in angle. For typical calculations, six grid points are used per decade in depth, 12 grid points are used per decade in energy, and 19 total grid points in angle. We also increase the energy resolution near the ion cyclotron resonance.

The temperature profile is initially assumed to be the grey profile,

$$T(\tau_R) = T_{\text{eff}} \left[ \frac{3}{4} \left( \tau_R + \frac{2}{3} \right) \right]^{1/4}. \quad (3.1)$$

The Rosseland mean depth  $\tau_R$  is given by  $d\tau_R = (\kappa^R / \kappa_0^{\text{sc}}) d\tau$ , where the Rosseland mean opacity is

$$\frac{1}{\kappa^R} = \frac{3\pi}{4\sigma_{\text{SB}} T^3} \int_0^\infty \frac{1}{2} \sum_j l_j \frac{\partial B_\nu}{\partial T} d\nu \quad (3.2)$$

and  $l_j$  is given by equation (2.23). Since  $l_j$  and  $\kappa^R$  are functions of  $\rho$  and  $T$  themselves, the profile (3.1) must be constructed by an iterative process: the temperature profile is first taken to be  $T(\tau) = T_{\text{eff}}[3/4(\tau + 2/3)]^{1/4}$ ; the density profile, and hence  $\kappa^{\text{tot}}$  and  $\kappa^R$ , are then determined, which allows the calculation of  $\tau_R(\tau)$ ; using equation (3.1) with this  $\tau_R$ , a revised temperature profile is obtained; the process is repeated until the new  $\tau_R(\tau)$  is not significantly different from the previous  $\tau_R(\tau)$ . To achieve  $|\Delta\tau/\tau|$  and  $|\Delta\tau_R/\tau_R| < 0.1$  per cent, three iterations are required.

To construct self-consistent atmosphere models requires successive global iterations, where the temperature profile  $T(\tau)$  is adjusted from the previous iteration to satisfy radiative equilibrium. At each global iteration, the profiles  $T(\tau)$  and  $\rho(\tau)$  are considered fixed. We solve the RTE (2.8) [see also equations (2.15)–(2.17)], together with the boundary conditions [see equations (2.9) and (2.10)] by the finite difference scheme described by Mihalas (1978). This results in a set of equations which have the form of a tridiagonal matrix that can be solved by the Feautrier procedure of forward-elimination and back-substitution. We have also implemented an improved Feautrier method to reduce errors



arising from machine precision as suggested by Rybicki & Hummer (1991). Note that, in the presence of scattering, the source function  $S_\nu^j$  [which involves mode coupling; see equation (2.16)] is not known prior to solving the RTE. We adopt the strategy that, for each global iteration,  $S_\nu^j$  is calculated using the solution for  $i_\nu^j$  from the previous global iteration, with  $S_\nu^j = B_\nu/2$  for the first global iteration. The full RTE is solved with this source function to obtain  $i_\nu^j$ , and the specific flux is calculated from finite differencing equation (2.7). Note that, unless the temperature correction from the previous iteration is relatively small, so that the source function calculated from the previous  $i_\nu^j$  approximates the true current source function, the global iteration may not converge.<sup>2</sup>

The current solution  $i_\nu^j$  does not, in general, satisfy the radiative equilibrium constraint nor does it yield a constant flux at every depth [see equations (2.13) and (2.14), respectively]. To satisfy both conditions requires correcting the temperature profile. We use a variation of the Unsöld–Lucy temperature correction method as described by Mihalas (1978) but modified to account for full radiative transfer by two propagation modes in a magnetic medium. The radiative equilibrium constraint given by equation (2.13) can be written as

$$\frac{dF_z}{d\tau} = c \left( \frac{\kappa^J}{\kappa_0^{\text{es}}} u - \frac{\kappa^P}{\kappa_0^{\text{es}}} u^P \right), \quad (3.3)$$

where  $u = \sum_{j=1}^2 \int d\nu u_\nu^j$  is the total radiation energy density,  $u^P = aT^4 = (4\sigma_{\text{SB}}/c)T^4$  is the blackbody energy density, and  $\kappa^J$  and  $\kappa^P$  are the absorption mean opacity and Planck mean opacity defined by

$$\kappa^J \equiv \frac{2}{cu} \sum_{j=1}^2 \int d\nu \int_+ d\mathbf{k} \kappa_f^{\text{abs}}(\mathbf{k}) i_\nu^j(\mathbf{k}), \quad (3.4)$$

$$\kappa^P \equiv \frac{1}{4\pi u^P} \sum_{j=1}^2 \int d\nu \int_+ d\mathbf{k} \kappa_f^{\text{abs}}(\mathbf{k}) u_\nu^j, \quad (3.5)$$

respectively. On the other hand, equation (2.7) can be integrated out formally to give  $i_\nu^j$  in terms of  $f_\nu^j$ , and we then have

$$\begin{aligned} cu(\tau) &= 2 \sum_{j=1}^2 \int d\nu \int_+ d\mathbf{k} i_\nu^j(\tau) \\ &= \int_0^\tau d\tau' \frac{\kappa^F(\tau')}{\kappa_0^{\text{es}}} F_z(\tau') + 2F_z(0), \end{aligned} \quad (3.6)$$

where we have used  $cu(0) \approx 2F_z(0)$ ,  $F_z(\tau)$  is the total flux at depth  $\tau$  (see equation 2.14), and  $\kappa^F(\tau)$  is the flux mean opacity defined by

$$\kappa^F \equiv \frac{2}{F_z} \sum_{j=1}^2 \int d\nu \int_+ d\mathbf{k} \frac{1}{\mu} \kappa_j^{\text{tot}}(\mathbf{k}) f_\nu^j(\mathbf{k}). \quad (3.7)$$

Combining equations (3.3) and (3.6) gives an expression for

<sup>2</sup> An alternative is to calculate  $S_\nu^j$  iteratively within each global iteration. The source function during each global iteration is first taken to be  $S_\nu^j = B_\nu/2$ , and thus the two modes are initially decoupled. The RTE is then solved for each mode  $j$ . The resulting  $i_\nu^j$  is used to determine a revised source function, which can then be reinserted into the RTE. This procedure is repeated until the source function converges, e.g.  $|\Delta S_\nu^j/S_\nu^j| < 5$  per cent. Obviously, this method requires longer computation time. In addition, we have implemented a procedure that reformulates the RTE using Eddington factors (see, e.g., Rybicki & Lightman 1979 for the analogous non-magnetic RTE using Eddington factors), but this does not lead to significant reduction in computation time.

$u^P[T(\tau)]$  in terms of  $F_z(\tau)$ . The desired temperature correction  $\Delta T(\tau)$  needed to satisfy radiative equilibrium is then

$$\begin{aligned} \Delta T(\tau) &\approx \frac{1}{16\sigma_{\text{SB}}T(\tau)^3} \left\{ -\frac{\kappa_0^{\text{es}}}{\kappa^P(\tau)} \frac{d[\Delta F_z(\tau)]}{d\tau} + \frac{\kappa^J(\tau)}{\kappa^P(\tau)} \right. \\ &\quad \times \left. \left[ \int_0^\tau d\tau' \frac{\kappa^F(\tau')}{\kappa_0^{\text{es}}} \Delta F_z(\tau') + 2\Delta F_z(0) \right] \right\}, \end{aligned} \quad (3.8)$$

where  $\Delta F_z(\tau) = \sigma_{\text{SB}}T_{\text{eff}}^4 - F_z(\tau)$ . Using equation (3.3) to replace  $dF_z/d\tau$  in equation (3.8), we obtain

$$\begin{aligned} \Delta T(\tau) &\approx \frac{1}{16\sigma_{\text{SB}}T(\tau)^3} \left\{ \frac{c}{\kappa^P(\tau)} [\kappa^J(\tau)u(\tau) - \kappa^P(\tau)u^P(\tau)] + \frac{\kappa^J(\tau)}{\kappa^P(\tau)} \right. \\ &\quad \times \left. \left[ \int_0^\tau d\tau' \frac{\kappa^F(\tau')}{\kappa_0^{\text{es}}} \Delta F_z(\tau') + 2\Delta F_z(0) \right] \right\}. \end{aligned} \quad (3.9)$$

Note that the first term in equation (3.9), which is  $\propto (\kappa^J u - \kappa^P u^P)$ , corresponds to the temperature correction in the  $\Lambda$ -iteration procedure  $\Delta T_\Lambda = (\kappa^J u - \kappa^P u^P)(\partial u^P/\partial T)^{-1}$  and is important near the surface but is small in the deeper layers where the atmosphere approaches a blackbody, while the remaining terms provide corrections in these deeper layers. In practice, we find that the Unsöld–Lucy temperature correction method as defined by equation (3.9) tends to overcorrect; therefore we only use  $\sim 70$ – $90$  per cent of the temperature correction. The process of determining the radiation intensity from the RTE for a given temperature profile, estimating and applying the temperature correction, and then recalculating the radiation intensity is repeated until convergence of the solution is achieved. We note here that, to decrease the number of iterations required for convergence and the total computation time, we can use as the initial temperature profile the result obtained from the diffusion calculation (see Section 3.2); such an initial temperature profile would already be close to radiative equilibrium.

Three criteria are used to indicate convergence. The first is that the temperature correction between successive global iterations becomes small, e.g.,  $|\Delta T/T| \lesssim 1$  per cent. The second is to check that radiative equilibrium (see equation 2.13) is sufficiently satisfied, or  $(\kappa^J u - \kappa^P u^P)/(\kappa^J u)$  is sufficiently small (see equation 3.3). The third criterion is that  $F_z$  is sufficiently close to  $\sigma_{\text{SB}}T_{\text{eff}}^4$  (see equation 2.14). Fig. 2 shows an example of these convergence tests after about 20 global iterations for our full radiative transport model of a fully ionized, pure H atmosphere with  $T_{\text{eff}} = 5 \times 10^6$  K,  $B = 10^{14}$  G, and  $\Theta_B = 0^\circ$ . Further iterations reduce the deviations, although the convergence is slower since the temperature corrections are already small. The numerical results presented in Section 4 have all reached the convergence level similar to Fig. 2.

### 3.2 Magnetic atmospheres with diffusion approximation

Using the diffusion approximation of radiative transport (see Section 2.3), we construct magnetic atmosphere models for general  $\Theta_B$ . We follow a similar procedure as the full radiative transfer method described in Section 3.1. We solve the approximate RTE (2.24) with boundary conditions given by equations (2.28) and (2.29) using the Feautrier method, which involves only depth and photon energy grid points. The modified Unsöld–Lucy temperature correction can be derived using the specific flux perpendicular to the stellar surface,  $F_{\nu,z}^j \approx -cl_j(\partial u_\nu^j/\partial z)$ , and equation (2.30). The resulting  $\Delta T(\tau)$  takes the same form as in equations (3.8) and (3.9),

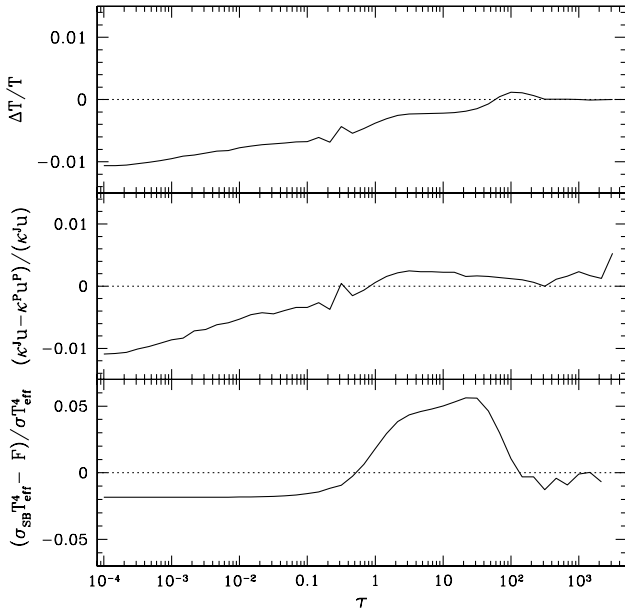


**Figure 2.** Convergence tests after  $\sim 20$  global iterations (temperature corrections) for a fully ionized H atmosphere model with  $T_{\text{eff}} = 5 \times 10^6$  K,  $B = 10^{14}$  G, and  $\Theta_B = 0^\circ$ . Fractional temperature correction (upper panel), deviation from radiative equilibrium [middle panel; see equations (3.3)–(3.5)], and deviation from constant total flux (lower panel) are plotted as functions of Thomson depth  $\tau$ . The larger deviations around  $\tau \sim 1$ –100 in the lower panel are because of the extraordinary-mode photons decoupling from the matter at  $\tau \sim 100$  (see Fig. 5); this region has the slowest convergence, but the deviations can be reduced further with additional iterations.

except that the mean opacities  $\kappa^J$ ,  $\kappa^P$ , and  $\kappa^F$  are given by

$$\kappa^J \equiv \frac{1}{u} \sum_{j=1}^2 \int d\nu K_j^{\text{abs}} u_{\nu}^j, \quad (3.10)$$

$$\kappa^P \equiv \frac{1}{2u^P} \sum_{j=1}^2 \int d\nu K_j^{\text{abs}} u_{\nu}^P, \quad (3.11)$$

and

$$\kappa^F \equiv \frac{1}{F_z} \sum_{j=1}^2 \int d\nu \frac{1}{\rho l_j} F_{\nu}^j, \quad (3.12)$$

respectively. The expressions for  $\kappa^J$  and  $\kappa^P$  are essentially the same as in Section 3.1. Atmosphere models for  $B \lesssim 10^{13}$  G based on the diffusion approximation have been constructed by Shibano et al. (1992) and Pavlov et al. (1995) using a different iteration scheme, i.e.  $\Lambda$ -iteration.

### 3.3 Non-magnetic atmospheres

For comparison, we also construct non-magnetic atmosphere models by solving the standard RTE (both full transport and in the diffusion approximation) using a similar method as described in Sections 3.1 and 3.2. In this case, the opacities are just due to non-magnetic electron scattering and free–free absorption. We implement the RTE with Eddington factors to determine the source function more accurately. We use the standard Feautrier method (with improvements described by Rybicki & Hummer 1991) and the standard Unsöld–Lucy temperature correction scheme described by Mihalas (1978).

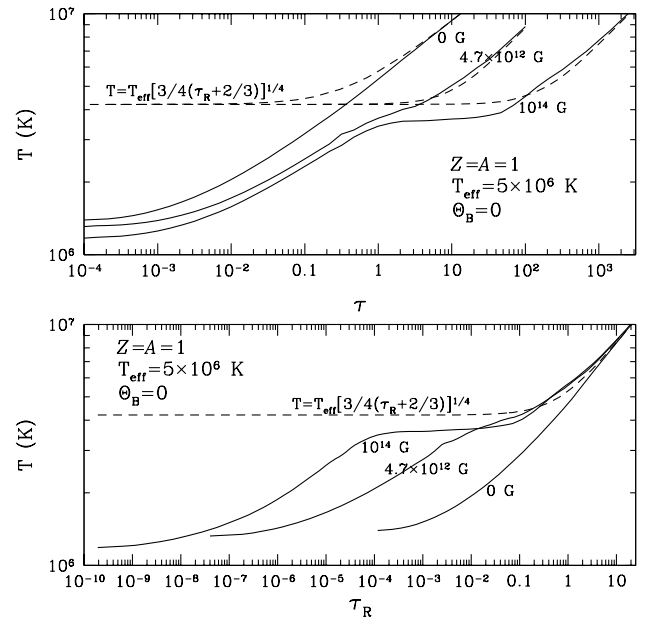


**Figure 3.** Temperature  $T$  as a function of Thomson depth  $\tau$  (upper panel) and Rosseland mean depth  $\tau_R$  (lower panel) for fully ionized, pure H atmospheres with  $T_{\text{eff}} = 5 \times 10^6$  K, and magnetic fields  $B = 0, 4.7 \times 10^{12}, 10^{14}$  G and  $\Theta_B = 0^\circ$ . The dashed lines show the grey temperature profile given by equation (3.1).

## 4 NUMERICAL RESULTS

### 4.1 Atmosphere structure

Fig. 3 shows the temperature profile as a function of Thomson depth  $\tau$  and Rosseland depth  $\tau_R$  for H atmospheres with  $T_{\text{eff}} = 5 \times 10^6$  K, magnetic fields  $B = 4.7 \times 10^{12}$  and  $10^{14}$  G, and the magnetic field oriented perpendicular to the surface ( $\Theta_B = 0^\circ$ ). For comparison, Fig. 3 also shows the temperature profile of our non-magnetic atmosphere model and the grey profile given by equation (3.1). Note that, since the Rosseland mean opacity (equation 3.2) is dominated by the (small) extraordinary-mode opacity, the Rosseland depth  $\tau_R(\tau)$  is significantly smaller at high fields than at  $B = 0$ . It is evident that all models approach the grey profile at  $\tau_R \gg 1$ , although this occurs deeper in the atmosphere for models with higher magnetic fields. At small depths of  $\tau \lesssim 1$ , the gas temperature is smaller, by a factor of a few, than predicted by the grey profile. This is because, for  $\tau \lesssim 1$ , the extraordinary-mode photons have already decoupled from the matter, and the temperature is primarily determined by the ordinary-mode absorption opacity, which is strongly non-grey ( $\kappa_2^{\text{abs}} \propto \nu^{-3}$  approximately). The plateau in the  $T(\tau)$  profile at  $\tau \sim 1$ –100 in the  $B = 10^{14}$  G model arises because the extraordinary-mode photons decouple from the matter at  $\tau \sim 100$  (see Section 4.2); such a plateau is more distinctive for high magnetic fields and becomes less pronounced for smaller magnetic fields.

Fig. 4 shows the temperature versus density profiles for various atmosphere models considered in this paper (see Section 4.3 for the spectral properties of these models). The plateau in temperature for the  $B = 10^{14}$  models corresponds to the similar feature shown in Fig. 3. Note that, in all models, the electrons are non-degenerate at the relevant densities, i.e.,  $T \gg T_F$  (see equation 2.38). Thus, even for high (quantizing) magnetic fields, the equation of state deviates from the classical ideal gas law by less than a few per cent (see Section 2.4). At a given  $B$ , the temperature profile,  $T(\tau)$ , of the He

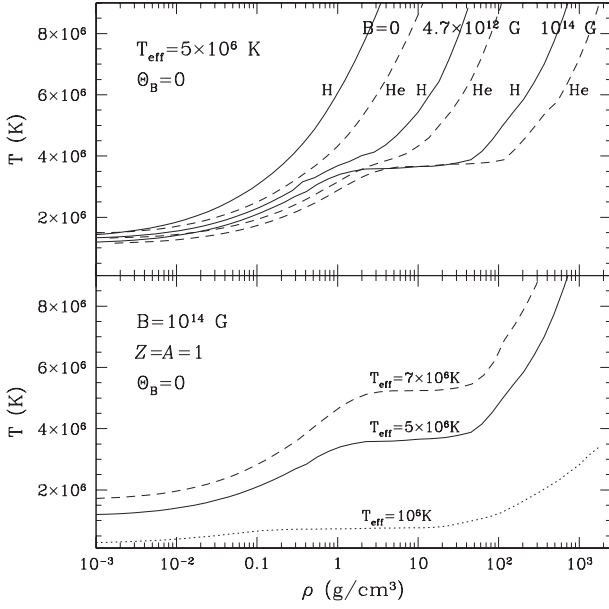


**Figure 4.** Temperature as a function of density for the various fully ionized atmosphere models considered in Section 4.3. The upper panel shows the H and He models at  $B = 0, 4.7 \times 10^{12}$ , and  $10^{14}$  G, all for  $T_{\text{eff}} = 5 \times 10^6$  K and  $\Theta_B = 0^\circ$ . The lower panel shows the H models at  $B = 10^{14}$  G for  $T_{\text{eff}} = 10^6, 5 \times 10^6$ , and  $7 \times 10^6$  K.

atmosphere is very close to that of the H atmosphere (see Fig. 3); this is expected since, apart from the ion cyclotron resonances, the H and He opacities have the same frequency dependence, and differ only by a factor of  $\sim 2$  in magnitude. With  $P \approx (1 + Z)\rho kT/A$ , we see that the He atmosphere has a higher density, by a factor of  $\sim 16/3$ , than the H atmosphere at the same temperature (see Fig. 4).

#### 4.2 Photon–matter decoupling region

To understand better the atmosphere structure and the emergent spectra (see Section 4.3), it is useful to develop a rough idea of the physical conditions in the region of the atmosphere where photons of different modes and energies decouple from the matter. Because of the angle dependence of the opacities, the exact location of the ‘decoupling layer’ is ambiguous. One possible approach is to use the averaged opacities defined in Section 2.3; the effective opacity for photon–matter energy exchange is  $K_j^{\text{eff}} = (K_j^{\text{abs}} \bar{K}_j^{\text{tot}})^{1/2}$  (see Rybicki & Lightman 1979), where  $\bar{K}_j^{\text{tot}} \equiv (\rho l_j)^{-1}$  and  $l_j$  and  $K_j^{\text{abs}}$  are given by equations (2.23) and (2.25), respectively. In fact, if mode coupling as a result of scattering is neglected, equation (2.24) can be approximately integrated out to yield  $u_j^i(y=0) \propto u_v^p(y \sim 1/K_j^{\text{eff}})$ , i.e., the emergent radiation density (of mode  $j$ ) is determined by the blackbody radiation density evaluated at the depth where the column density  $y \sim 1/K_j^{\text{eff}}$ . We therefore define the effective optical depth:

$$\tau_{vj}^{\text{eff}}(\tau) = \frac{1}{\kappa_0^{\text{es}}} \int_0^\tau d\tau' (K_j^{\text{abs}} \bar{K}_j^{\text{tot}})^{1/2} = \frac{1}{\kappa_0^{\text{es}}} \int_0^\tau d\tau' \left( \frac{K_j^{\text{abs}}}{\rho l_j} \right)^{1/2}, \quad (4.1)$$

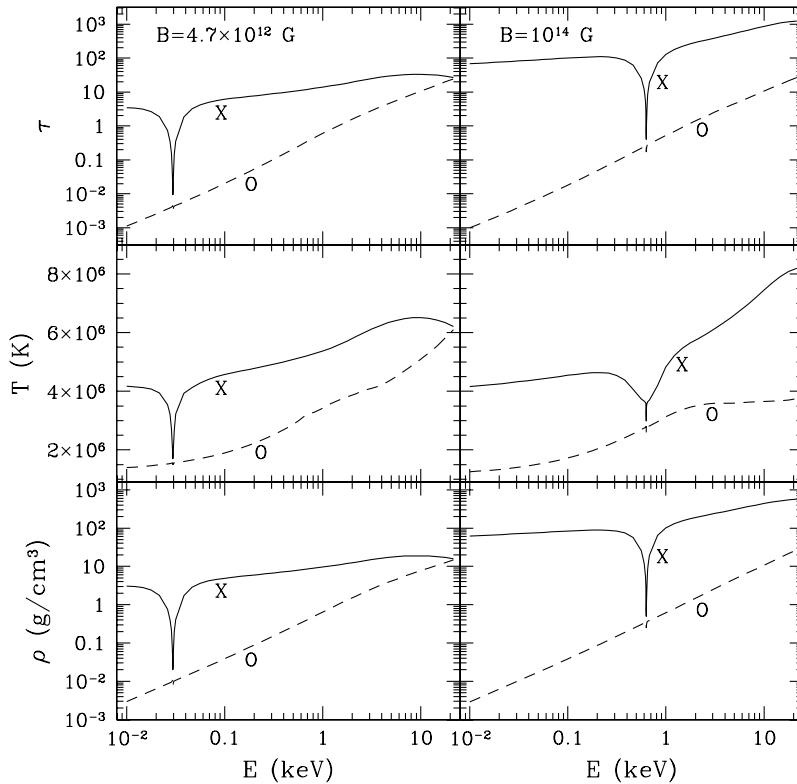


**Figure 5.** The upper panels show the Thomson depth at which photons decouple from the matter [effective optical depth  $\tau_{vj}^{\text{eff}} = 1$ ; see equation (4.1)] as a function of energy for the  $T_{\text{eff}} = 5 \times 10^6$  K,  $\Theta_B = 0^\circ$ , and  $B = 4.7 \times 10^{12}$  (left panels) and  $10^{14}$  G (right panels) atmosphere models. Also plotted are the local temperature  $T$  (middle panels) and density  $\rho$  (lower panels) at these Thomson depths. The solid lines are for the extraordinary mode ( $j = 1$ ), and the dashed lines are for the ordinary mode ( $j = 2$ ).

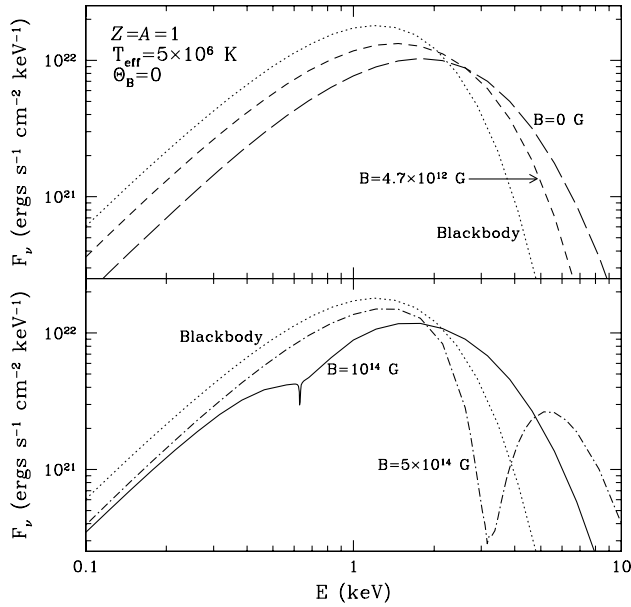


**Figure 6.** Spectra of NS atmospheres with fully ionized hydrogen at  $T_{\text{eff}} = 5 \times 10^6$  K and  $\Theta_B = 0^\circ$ . The dot-dashed line is for the  $B = 5 \times 10^{14}$  G atmosphere, the solid line is for the  $B = 10^{14}$  G atmosphere, the short-dashed line is for the  $B = 4.7 \times 10^{12}$  G atmosphere, the long-dashed line is for the non-magnetic atmosphere, and the dotted lines are for a blackbody with  $T = 5 \times 10^6$  K. At  $B = 5 \times 10^{14}$  G, the  $E_{Bi} = 3.15$  keV ion cyclotron feature (from  $\sim 2$  to  $\sim 5$  keV) has an equivalent width  $\sim 1.9$  keV, while at  $B = 10^{14}$  G, the  $E_{Bi} = 0.63$  keV feature (from  $\sim 0.4$  to  $\sim 1$  keV) has an equivalent width  $\sim 90$  eV. Note that the extremely narrow natural/thermal lines at  $E_{Bi}$  have negligible equivalent widths.

so that photons of mode  $j$  and frequency  $\nu$  decouple from the matter at  $\tau_{\nu j}^{\text{eff}} \sim 1$ . Fig. 5 shows the Thomson depth and local temperature and density as functions of photon energy at the decoupling layer for the H atmosphere model with  $T_{\text{eff}} = 5 \times 10^6$  K,  $\Theta_B = 0^\circ$ , and  $B = 4.7 \times 10^{12}$  and  $10^{14}$  G (see also Fig. 3). Note that the effective depth defined in equation (4.1) errs for photons propagating along the magnetic field since the opacities are generally lower near  $\theta_B = 0$ ; hence, these photons decouple from the matter at deeper layers than those indicated in Fig. 5. Nevertheless, Fig. 5 gives the typical conditions where the observed photons of energy  $E$  are generated. It is clear that the extraordinary-mode photons can emerge from deep in the atmosphere where plasma effects on the opacities are not negligible (see Section 2.5 and Fig. 1). Photons with energies near the ion cyclotron resonance  $E_{Bi} = 0.63 B_{14}$  keV decouple in the lower temperature region; this gives rise to the absorption feature in the emergent radiation spectrum (see Section 4.3).

### 4.3 Spectra

Fig. 6 shows the spectra of the H atmospheres with  $T_{\text{eff}} = 5 \times 10^6$  K,  $\Theta_B = 0^\circ$ , and magnetic fields of  $B = 4.7 \times 10^{12}$ ,  $10^{14}$ , and  $5 \times 10^{14}$  G. Also plotted are the spectrum of our non-magnetic fully ionized H atmosphere model and the blackbody spectrum at  $T = 5 \times 10^6$  K. The spectra clearly show a significantly harder high-energy tail and a depletion of low-energy photons relative to the blackbody. For example, in the case of  $B = 10^{14}$  G, the flux at  $E = 5$  keV is an order of magnitude larger than the corresponding blackbody flux. At a given energy  $E$  (and for the same  $T_{\text{eff}}$ ), the flux depends on the field strength in a non-monotonic fashion for the models depicted in Fig. 6. For

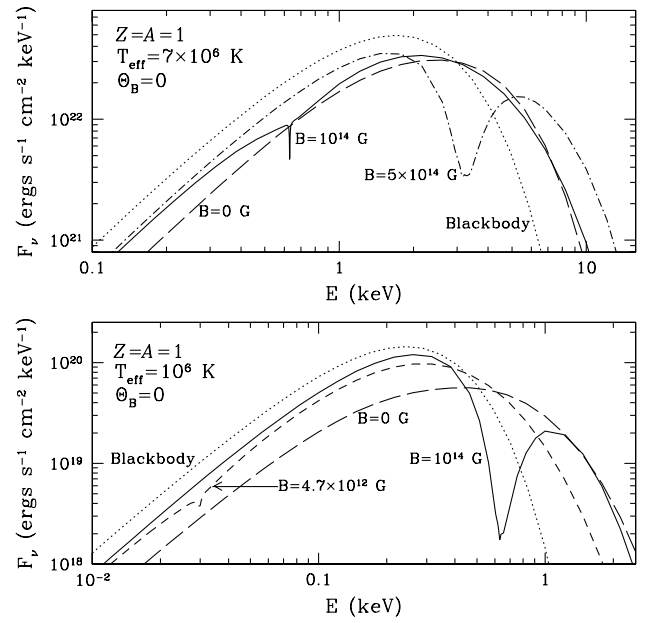


**Figure 7.** Spectra of NS atmospheres with fully ionized hydrogen at  $T_{\text{eff}} = 7 \times 10^6$  K (upper panel) and  $10^6$  K (lower panel) and  $\Theta_B = 0^\circ$ . The dot-dashed line is for the  $B = 5 \times 10^{14}$  G atmosphere, the solid lines are for the  $B = 10^{14}$  G atmosphere, the short-dashed line is for the  $B = 4.7 \times 10^{12}$  G atmosphere, the long-dashed lines are for the nonmagnetic atmosphere, and the dotted lines are for a blackbody with  $T = 7 \times 10^6$  and  $10^6$  K. Note that the ion cyclotron resonance features are more pronounced when  $E_{Bi} \geq 3kT_{\text{eff}}$ : at  $B = 5 \times 10^{14}$  G and  $T_{\text{eff}} = 7 \times 10^6$  K, the  $E_{Bi} = 3.15$  keV feature (from  $\sim 2$  to  $\sim 5$  keV) has an equivalent width  $\sim 1.8$  keV, while at  $B = 10^{14}$  G and  $T_{\text{eff}} = 10^6$  K, the  $E_{Bi} = 0.63$  keV feature (from  $\sim 0.4$  to  $\sim 1$  keV) has an equivalent width  $\sim 0.4$  keV. Also note that the extremely narrow natural/thermal lines at  $E_{Bi}$  have negligible equivalent widths.

example, at  $E = 7$  keV, the flux increases in the order of  $B = 4.7 \times 10^{12}$ ,  $10^{14}$ ,  $0.5 \times 10^{14}$  G. The hard tails were already noted in previous studies of NS atmospheres with  $B \leq 10^{13}$  G (e.g. Pavlov et al. 1995; see also references cited in Section 1), and they arise because high-energy photons have smaller opacities and thus decouple from deeper, hotter layers (see Fig. 5). It is evident that fitting the high-energy tail of observations with a blackbody will yield overestimates of the surface temperature of the NS.

Most prominent in the spectra of highly magnetized atmospheres is the absorption feature at the ion cyclotron resonance  $E_{Bi} = 0.63(Z/A)B_{14}$  keV. This can be directly traced back to the corresponding resonance feature in the opacities (see Fig. 1). The ion cyclotron feature is broad, with  $\Delta E/E_{Bi} \sim 1$ , and is much broader than the natural or thermal width of the line [see Section 2.6 for a discussion and equation (2.69) in particular].<sup>3</sup> We find that the ion cyclotron feature is most pronounced when it appears beyond the blackbody peak, i.e., when  $E_{Bi} \geq 3kT_{\text{eff}}$ . For the models depicted in Fig. 6, the equivalent width of the  $E_{Bi} = 3.15$ -keV line at  $B_{14} = 5$  is about 1.9 keV, the 0.63-keV line at  $B_{14} = 1$  is 90 eV, and the 29.6-eV line (not shown) at  $B_{12} = 4.7$  is only 1.3 eV.

Fig. 7 shows the spectra of H atmospheres at two different effective temperatures:  $T_{\text{eff}} = 10^6$  and  $7 \times 10^6$  K. The spectra are

<sup>3</sup> In discussing the cyclotron feature in this paper, we are referring to the broad depletion of flux around the ion cyclotron energy rather than the very narrow ( $\Delta E/E \sim 10^{-3}$ ) natural/thermal line; such a line has negligible equivalent width and is not always resolved in Figs 7–9 and 11.



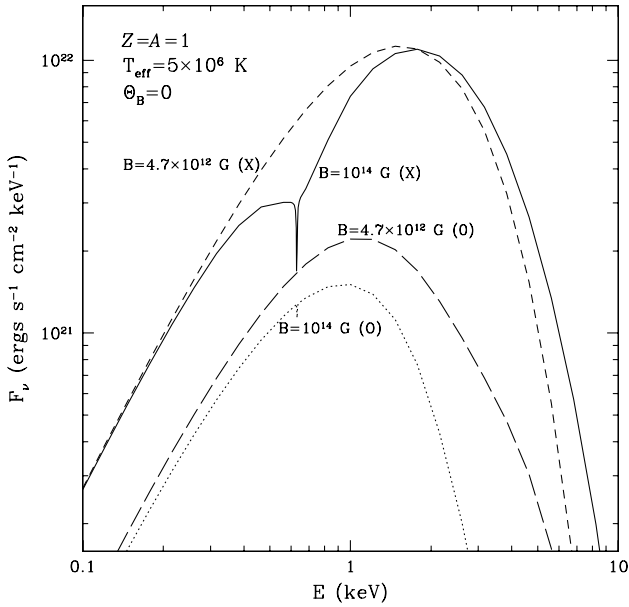


**Figure 8.** Spectra of NS atmospheres with fully ionized hydrogen at  $T_{\text{eff}} = 5 \times 10^6$  K and  $\Theta_B = 0^\circ$ . The solid and dotted lines are for the  $B = 10^{14}$  G extraordinary mode ( $j = 1$ ) and ordinary mode ( $j = 2$ ), respectively, and the short and long-dashed lines are for the  $B = 4.7 \times 10^{12}$  G extraordinary and ordinary modes, respectively.

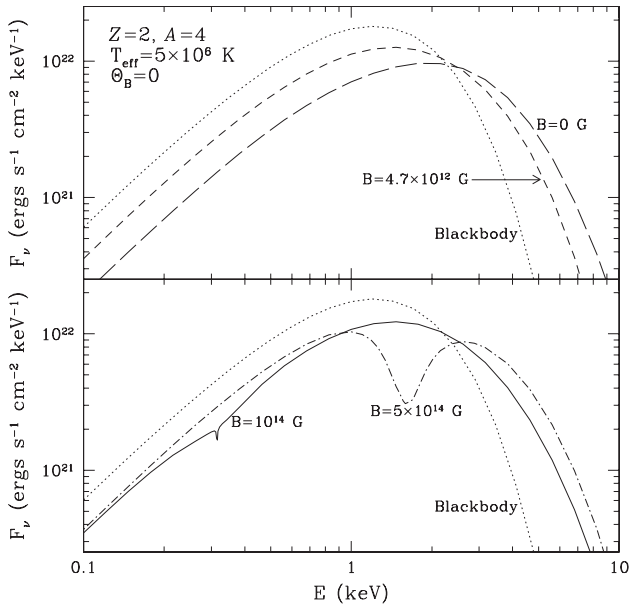


**Figure 9.** Spectra of NS atmospheres with fully ionized helium at  $T_{\text{eff}} = 5 \times 10^6$  K and  $\Theta_B = 0^\circ$ . The dot-dashed line is for the  $B = 5 \times 10^{14}$  G atmosphere, the solid line is for the  $B = 10^{14}$  G atmosphere, the short-dashed line is for the  $B = 4.7 \times 10^{12}$  G atmosphere, the long-dashed line is for the non-magnetic atmosphere, and the dotted lines are for a blackbody with  $T = 5 \times 10^6$  K. At  $B = 5 \times 10^{14}$  G, the  $E_{Bi} = 1.58$  keV ion cyclotron feature (from  $\sim 1$  to  $\sim 2$  keV) has an equivalent width  $\sim 0.51$  keV, while at  $B = 10^{14}$  G, the  $E_{Bi} = 0.32$  keV feature (from  $\sim 0.2$  to  $\sim 0.4$  keV) has an equivalent width  $\sim 10$  eV.

similar to those of the  $T_{\text{eff}} = 5 \times 10^6$  K models shown in Fig. 6. The cyclotron resonance at 0.63 keV (for  $B_{14} = 1$ ) becomes prominent for  $T_{\text{eff}} = 10^6$  K since the condition  $E_{Bi} \approx 3kT_{\text{eff}}$  is satisfied. Note that the  $T_{\text{eff}} = 10^6$  K models should be considered for illustrative purposes only since we expect the opacities to be

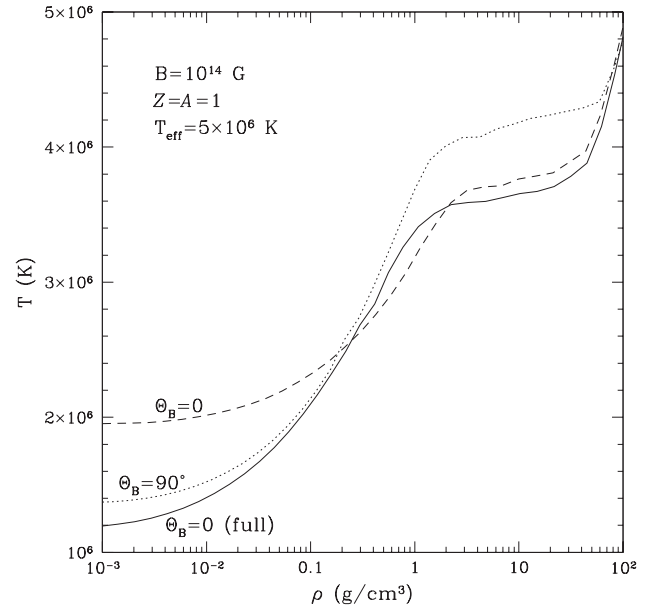


**Figure 10.** Comparison of the temperature–density profiles between the full radiative transport and diffusion approximated transport models considered in Section 4.4. The solid line is for  $\Theta_B = 0^\circ$  (full radiative transport), the dashed line is for  $\Theta_B = 0^\circ$  (diffusion), and the dotted line is for  $\Theta_B = 90^\circ$  (diffusion).

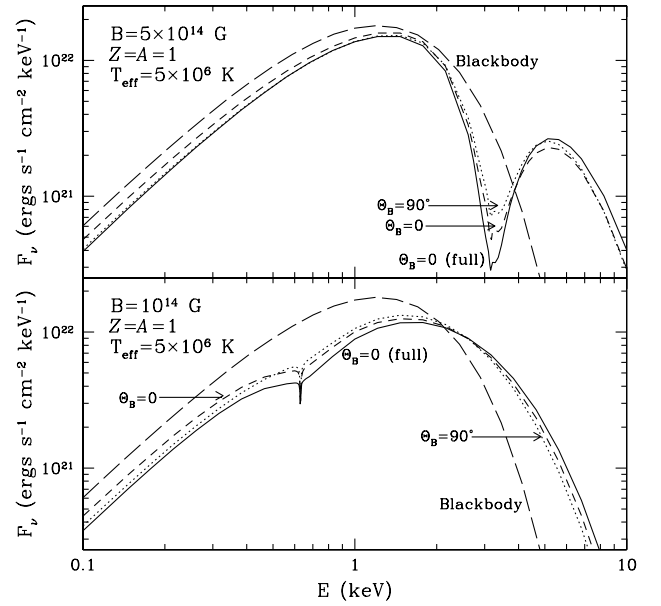


**Figure 11.** Spectra of NS atmospheres with fully ionized hydrogen at  $B = 5 \times 10^{14}$  (upper panel) and  $10^{14}$  G (lower panel) and  $T_{\text{eff}} = 5 \times 10^6$  K. The solid lines are for  $\Theta_B = 0^\circ$  (full radiative transport), the short-dashed lines are for  $\Theta_B = 0^\circ$  (diffusion), the dotted lines are for  $\Theta_B = 90^\circ$  (diffusion), and the long-dashed lines are for a blackbody with  $5 \times 10^6$  K.

significantly modified by neutral atoms and even molecules at such a low temperature (see Section 5).

As noted before, in strong magnetic fields, the thermal radiation is primarily carried by the extraordinary-mode photons. This can be seen clearly in Fig. 8. Obviously the emergent radiation is expected to be polarized. Also note that the ion cyclotron resonance feature occurs only for the extraordinary mode, as expected from the behaviour of the opacities (see Sections 2.5 and 2.6).

Fig. 9 shows the spectra of the He atmospheres with  $T_{\text{eff}} = 5 \times 10^6$  K,  $\Theta_B = 0^\circ$ , and magnetic fields of  $B = 0, 4.7 \times 10^{12}, 10^{14}$  and  $5 \times 10^{14}$  G. These should be compared to the spectra of H atmospheres shown in Fig. 6. Although the He atmosphere is denser than the H atmosphere (see Section 4.1 and Fig. 4), there is no clear distinction between their spectra except for the ion cyclotron resonance features. For example, at  $B = 10^{14}$  G and  $T_{\text{eff}} = 5 \times 10^6$  K, the flux of the He atmosphere at  $E = 6$  keV is lower than that of the H atmosphere by only a factor of 1.2. Clearly, it would be difficult to distinguish a H atmosphere from a He atmosphere based on spectral information in the 1–10 keV band alone. We also note that the equivalent widths of the ion cyclotron features for the He atmospheres are about 0.51 keV for the  $E_{Bi} = 1.58$ -keV line at  $B_{14} = 5$  and about 10 eV for the  $E_{Bi} = 0.32$ -keV line at  $B_{14} = 1$ .

#### 4.4 Full radiative transport versus diffusion approximation

The atmosphere models presented in Sections 4.1–4.3 are based on solutions of the full RTEs (see Sections 2.1 and 3.1). These models are currently restricted to the case where the magnetic field is perpendicular to the stellar surface, i.e.  $\Theta_B = 0^\circ$ . Using the diffusion approximation (see Sections 2.3 and 3.2), we construct atmosphere models for general  $\Theta_B$ s.

Fig. 10 shows the temperature–density profiles of the H atmosphere models with  $B = 10^{14}$  G,  $T_{\text{eff}} = 5 \times 10^6$  K, and  $\Theta_B = 0^\circ$  and  $90^\circ$  based on the diffusion approximation. These are compared with the result of the corresponding full transport model with  $\Theta_B = 0^\circ$ . Clearly, in the diffusion models, the surface temperature (where  $\rho \lesssim 0.01$  g cm $^{-3}$ ) for  $\Theta_B = 90^\circ$  is significantly less than for  $\Theta_B = 0^\circ$  (by roughly a factor of 1.4 for the models considered here); this was already noted by Pavlov et al. (1995) and Shibano et al. (1992) for the  $B \sim 10^{12}$  G models. At  $10^{14}$  G, the temperature plateaus (as a result of the decoupling of the extraordinary-mode photons; see Section 4.1) are also different for  $\Theta_B = 0^\circ$  and  $90^\circ$ . The difference in the temperature profiles for different magnetic field geometries implies that different parts of the NS surface will have different temperatures, e.g., the magnetic equator is cooler than the magnetic poles, even if  $T_{\text{eff}}$  is uniform. Clearly, a full understanding of the NS surface temperature distribution requires detailed modelling of the three-dimensional atmosphere and of the anisotropic heat transport through the NS crust; this is beyond the scope of this paper. Comparing the diffusion model with the full transport model, we see from Fig. 10 that, at  $\Theta_B = 0^\circ$ , the temperature in the full model is significantly lower than that of the diffusion model in the outermost layers of the atmosphere.

Fig. 11 shows that, despite the difference in the temperature profiles, the spectra of the diffusion models for  $\Theta_B = 0^\circ$  and  $90^\circ$  and the spectra of the full transport model are rather similar. For  $B_{14} = 1$ , the equivalent width of the cyclotron feature at  $E_{Bi} = 0.63$  keV is about 80 eV for  $\Theta_B = 0^\circ$  and 50 eV for  $\Theta_B = 90^\circ$ , while for  $B_{14} = 5$ , the feature at  $E_{Bi} = 3.15$  keV has a width of about 1.9 keV for  $\Theta_B = 0^\circ$  and  $90^\circ$ . We also find that the polarized emission is stronger for  $\Theta_B = 90^\circ$  than for  $0^\circ$ , as already noted by Shibano et al. (1992) for the  $B = 4.7 \times 10^{12}$  G models.

## 5 DISCUSSION

In this paper, we have constructed models of magnetized NS atmospheres composed of ionized hydrogen or helium. We focused on the superstrong field regime ( $B \gtrsim 10^{14}$  G) as directly relevant to

magnetars (see Section 1). We solve the full, angle-dependent RTEs for the coupled polarization modes and include the ion cyclotron and plasma effects on the opacities and polarization modes. Since the magnetic field greatly suppresses the opacities of the extraordinary-mode photons, the thermal radiation emerges from deep in the atmosphere ( $\rho \sim 10^2$  g cm $^{-3}$  for  $B = 10^{14}$  G), where the medium effect is non-negligible. As already noted in previous works on NS atmospheres with moderate ( $\sim 10^{12}$  G) or negligible magnetic fields, the thermal emission from a highly magnetized NS is polarized, with the spectrum harder than the blackbody. We find that the ion cyclotron resonance, at  $E_{Bi} = 0.63(Z/A)(B/10^{14} \text{ G})$  keV, can give rise to a broad ( $\Delta E/E \sim 1$ ) and potentially observable absorption feature in the spectrum, especially when  $E_{Bi} \gtrsim 3kT_{\text{eff}}$ . Clearly the detection of such a feature would provide an important diagnostic for magnetars.

We note that the spectra presented in this paper (see Figs 6–9 and 11) correspond to emission from a local patch of the NS surface. To compare directly with observations, one must calculate synthetic spectra from the whole stellar surface, taking into account the effect of gravitational redshift and light-bending. To do this, one must know the distribution of the magnetic field (both magnitude and direction) and the effective temperature over the stellar surface. For a given field geometry, the surface temperature distribution may be obtained from crustal heat conduction calculations (e.g. Hernquist 1985; Schaaf 1990; Page 1995; Heyl & Hernquist 1998), but this is intrinsically coupled to the properties of the atmosphere; the problem is further complicated by the existence of lateral radiative flux (see Section 2.3) and the non-uniform temperature distribution induced by the magnetic field in the atmosphere (see Section 4.4). Obviously we expect the cyclotron feature to be broadened and less deep if different parts of the surface with different field strengths contribute similarly to the observed flux (see Zane et al. 2001 for a calculation based on a dipole field and an approximate temperature distribution).

Several physical effects have been neglected in our atmosphere models (see Özel 2001; Zane et al. 2001, for related works on magnetar atmospheres; see also Section 1 for references of previous works). We have assumed that the atmosphere is fully ionized. The problem of ionization equilibrium in a highly magnetized medium is a complicated one owing to the non-trivial coupling between the centre-of-mass motion and the internal atomic structure and to the relatively high densities of the atmosphere (see Lai 2001 and references therein). While estimates based on the calculations of Potekhin et al. (1999) indicate that the fraction of neutral atoms is no more than a few per cent for  $T \gtrsim 5 \times 10^6$  K at  $B \sim 10^{14}$  G, it should be noted that even a small neutral fraction can potentially affect the radiative opacities. For example, the ionization edge of a stationary H atom (in the ground state) occurs at energy  $E_i \approx 4.4(\ln b)^2$  eV, where  $b \equiv B/(2.35 \times 10^9 \text{ G})$  (thus,  $E_i = 0.16, 0.31, 0.54, 0.87$  keV for  $B = 10^{12}, 10^{13}, 10^{14}, 10^{15}$  G, respectively; see Lai 2001). The ratio of the free–free and bound–free opacities (for the extraordinary mode) at  $E = E_i$  is of order  $10^{-6} \rho_1 / (T_6^{1/2} B_{14} f_H)$ , where  $\rho_1 = \rho/(1 \text{ g cm}^{-3})$ ,  $T_6 = T/(10^6 \text{ K})$ ,  $B_{14} = B/(10^{14} \text{ G})$ , and  $f_H$  is the fraction of H atoms in the ‘centred’ ground state (see Lai 2001). Thus one could in principle expect atomic features, broadened by the ‘motional Stark effect,’ in the spectra; these could blend with the ion cyclotron feature, at  $E_{Bi}$ , studied in this paper.

Another caveat of our models is the neglect of the vacuum polarization effect. In a strong magnetic field, vacuum polarization (in which photons are temporarily converted into electron–positron

pairs) contributes to the refractive index by a term of order  $\delta_{\nu p} = (\alpha_F/45\pi)(B/B_Q)^2$ , where  $\alpha_F = 1/137$  and  $B_Q = 4.4 \times 10^{13}$  G, and the effect tends to induce linear polarization of the modes (Adler 1971). Thus for  $3\delta_{\nu p} \approx (\omega_p/\omega)^2$  (where  $\omega_p$  is the electron plasma frequency), or, for photon energies  $\hbar\omega \approx \hbar\omega_{\nu p} = (15\pi/\alpha_F)^{1/2}(\omega_p/\omega_{Be})m_e c^2 = 1.0\rho_1^{1/2}B_{14}^{-1}$  keV,<sup>4</sup> the normal modes (and thus the radiative opacities) are modified by vacuum polarization (e.g. Gnedin, Pavlov & Shibano 1978; Mészáros & Ventura 1979). Previous works (see Mészáros 1992 for a review; see also Shibano et al. 1992; Özel 2001 for atmosphere models that include the vacuum polarization effect; note that Özel 2001 studied the  $B \gg B_Q$  regime but used the vacuum polarization expressions valid only for  $B \ll B_Q$ ) neglected the response of the ions in calculating the dielectric tensor. However, as shown in this paper, for  $B \approx 10^{14}$  G, the ion cyclotron resonance gives rise to a prominent feature in the polarization mode vector and in the opacities. Therefore one must consider the combined system of electrons, ions, and polarized vacuum in order to model the spectra in the superstrong field regime (Ho & Lai, in preparation). Also, vacuum polarization causes the opacities to exhibit a resonance feature at  $E = \hbar\omega_{\nu p}$  (Pavlov & Shibano 1979; Ventura et al. 1979; see Mészáros 1992 for a review). Since  $\hbar\omega_{\nu p} \propto \rho^{1/2}$  and since atmosphere models necessarily require discrete depth (density) and energy grid points, such features can appear in the model spectra, while, in a real atmosphere, they will be smoothed out. Moreover, vacuum polarization can induce resonant mode conversion which may significantly affect the radiation transport (Lai & Ho 2001). We will present atmosphere models including vacuum polarization in a future work (Ho & Lai, in preparation).

Finally, although in this paper we have included the medium effect on the polarization modes (see Section 2.5), at sufficiently high densities or low photon energies, the refractive index of the medium deviates from unity or even becomes complex. This will introduce additional effects on the radiative transport and the resulting spectra. This issue will be addressed in a future work.

## ACKNOWLEDGMENTS

We would like to express our appreciation to Roberto Turolla for his careful reading of the manuscript and his suggestions and comments. DL thanks Feryal Özel for discussions of her work at the ITP conference ‘Spin and Magnetism in Young Neutron Stars’ held in 2000 October. This work was supported in part by NASA Grant NAG 5-8484 and NAG 5-8356 and NSF grant AST 9986740. DL was also supported by a fellowship from the A.P. Sloan foundation.

## REFERENCES

- Adler S. L., 1971, *Ann. Phys.*, **67**, 599  
 Alcock C., Illarionov A., 1980, *ApJ*, **235**, 534  
 Alpar M. A., 2001, *ApJ*, **554**, 1245  
 Antia H. M., 1993, *ApJS*, **84**, 101  
 Becker W., 2000, in Martens P. C. H., Tsuruta S., Weber M. A., eds, *Proc. IAU Symp. 195, Highly Energetic Physical Processes and Mechanisms for Emission from Astrophysical Plasmas*. Astron. Soc. Pac., San Francisco, p. 49  
 Becker W., Trümper J., 1997, *A&A*, **326**, 682

- Bulik T., Pavlov G. G., 1996, *ApJ*, **469**, 373  
 Caraveo P. A., 1998, *Advances in Space Research*, **21**, 187  
 Caraveo P. A., Bignami G. F., Trümper J., 1996, *A&AR*, **7**, 209  
 Caraveo P. A., Mignani R. P., Pavlov G. G., Bignami G. F., 2000, *Proc. A Decade of HST Science*. Baltimore, in press (astro-ph/0008523)  
 Chatterjee P., Hernquist L., Narayan R., 2000, *ApJ*, **534**, 373  
 Duncan R. C., Thompson C., 1992, *ApJ*, **392**, L9  
 Edelstein J., Foster R. S., Bowyer S., 1995, *ApJ*, **454**, 442  
 Ginzburg V. L., 1970, *Propagation of Electromagnetic Waves in Plasmas*. 2nd edn. Pergamon Press, Oxford  
 Gnedin Yu. N., Pavlov G. G., 1974, *Sov. Phys. JETP*, **38**, 903  
 Gnedin Yu. N., Pavlov G. G., Shibano Yu. A., 1978, *Sov. Astron. Lett.*, **4**, 117  
 Hernquist L., 1985, *MNRAS*, **213**, 313  
 Heyl J. S., Hernquist L., 1997a, *ApJ*, **489**, L67  
 Heyl J. S., Hernquist L., 1997b, *J. Phys. A*, **30**, 6485  
 Heyl J. S., Hernquist L., 1998, *MNRAS*, **300**, 599  
 Hulleman F., van Kerkwijk M. H., Kulkarni S. R., 2000, *Nat*, **408**, 689  
 Hurley K., 2000, in Kippen R. M., Mallozzi R. S., Fishman G. J., eds, *Gamma-Ray Bursts: Fifth Huntsville Symposium*, AIP Conf. Proc. 526. Am. Inst. Phys., New York  
 Kaminker A. D., Pavlov G. G., Shibano Yu. A., 1982, *Ap&SS*, **86**, 249  
 Kaminker A. D., Pavlov G. G., Shibano Yu. A., 1983, *Ap&SS*, **91**, 167  
 Kaplan D. L., Kulkarni S. R., van Kerkwijk M. H., Rothschild R. E., Lingelfelter R. L., Marsden D., Danner R., Murakami T., 2001, *ApJ*, **556**, 399  
 Kaspi V. M., Gavril F. P., Chakrabarty D., Lackey J. R., Muno M. P., 2001, *ApJ*, in press (astro-ph/0011368)  
 Korpela E. J., Bowyer S., 1998, *AJ*, **115**, 2551  
 Kouveliotou C. et al., 1998, *Nat*, **393**, 235  
 Kouveliotou C. et al., 1999, *ApJ*, **510**, L115  
 Lai D., 2001, *Rev. Mod. Phys.*, **73**, in press (astro-ph/0009333)  
 Lai D., Ho W. C. G., 2001, *ApJL*, submitted (astro-ph/0108127)  
 Lai D., Salpeter E. E., 1997, *ApJ*, **491**, 270  
 Mereghetti S., 1999, review presented at NATO ASI ‘Neutron Star-Black Hole Connection’ (astro-ph/9911252)  
 Mészáros P., 1992, *High-Energy Radiation from Magnetized Neutron Stars*. Univ. Chicago Press, Chicago  
 Mészáros P., Ventura J., 1979, *Phys. Rev. D*, **19**, 3565  
 Meyer R. D., Pavlov G. G., Mészáros P., 1994, *ApJ*, **433**, 265  
 Mignani R., Caraveo P. A., Bignami G. E., 1998, *Advances in Space Research*, **21**, 197  
 Mihalas D., 1978, *Stellar Atmospheres*. 2nd edn. W.H. Freeman and Co., San Francisco  
 Miller M. C., 1992, *MNRAS*, **255**, 129  
 Nagel W., 1980, *ApJ*, **236**, 904  
 Nagel W., Ventura J., 1983, *A&A*, **118**, 66  
 Özel F., 2001, *ApJ*, submitted (astro-ph/0103227)  
 Paerels F. et al., 2001, *A&A*, **365**, L298  
 Page D., 1995, *Space Sci. Rev.*, **74**, 437  
 Pavlov G., 2000, [http://online.itp.ucsb.edu/online/neustars\\_c00/pavlov/](http://online.itp.ucsb.edu/online/neustars_c00/pavlov/)  
 Pavlov G. G., Panov A. N., 1976, *Sov. Phys. JETP*, **44**, 300  
 Pavlov G. G., Shibano Yu. A., 1979, *Sov. Phys. JETP*, **49**, 741  
 Pavlov G. G., Zavlin V. E., 2000, *ApJ*, **529**, 1011  
 Pavlov G. G., Shibano Yu. A., Ventura J., Zavlin V. E., 1994, *A&A*, **289**, 837  
 Pavlov G. G., Shibano Yu. A., Zavlin V. E., Meyer R. D., 1995, in Alpar M. A., Kiziloglu U., van Paradijs J., eds, *Lives of the Neutron Stars*. Kluwer Academic, Boston, p. 71  
 Pavlov G. G., Zavlin V. E., Trümper J., Neuhäuser R., 1996, *ApJ*, **472**, L33  
 Pavlov G. G., Welty A. D., Cordova F. A., 1997, *ApJ*, **489**, L75  
 Perna R., Heyl J. S., Hernquist L. E., Juett A. M., Chakrabarty D., 2001, *ApJ*, **557**, 18  
 Potekhin A. Y., Chabrier G., Shibano Yu. A., 1999, *Phys. Rev. E*, **60**, 2193  
 Rajagopal M., Romani R. W., 1996, *ApJ*, **461**, 327  
 Rajagopal M., Romani R. W., Miller M. C., 1997, *ApJ*, **479**, 347

<sup>4</sup>The expressions of  $\delta_{\nu p}$  and  $\hbar\omega_{\nu p}$  given here are valid for  $B \ll B_Q$ . The use of more general expressions (Tsai & Erber 1975; Heyl & Hernquist 1997b) results in different scalings with  $B$ , and the numerical values differ by a factor of a few for  $B \sim 10^{14}$ – $10^{15}$  G (Ho & Lai, in preparation).

- Romani R. W., 1987, *ApJ*, 313, 718  
 Rybicki G. B., Hummer D. G., 1991, *A&A*, 245, 171  
 Rybicki G. B., Lightman A. P., 1979, *Radiative Processes in Astrophysics*. John Wiley & Sons, New York  
 Schaaf M. E., 1990, *A&A*, 227, 61  
 Shafranov V. D., Leontovich M. A. 1967, *Reviews of Plasma Physics*, Vol. 3. Consultants Bureau, New York  
 Shapiro S. L., Teukolsky S. A., 1983, *Black Holes, White Dwarfs, and Neutron Stars*. John Wiley & Sons, New York  
 Shibano Yu. A., Zavlin V. E., 1995, *Astron. Lett.*, 21, 3  
 Shibano Yu. A., Zavlin V. E., Pavlov G. G., Ventura J., 1992, *A&A*, 266, 313  
 Thompson C., 2000, in Connaughton V. et al., eds, *NATO ASI, Neutron Star-Black Hole Connection*. Kluwer, Dordrecht, in press (astro-ph/0010016)  
 Thompson C., Blaes O., 1998, *Phys. Rev. D*, 57, 3219  
 Thompson C., Duncan R. C., 1993, *ApJ*, 408, 194  
 Thompson C., Duncan R. C., 1995, *MNRAS*, 275, 255  
 Thompson C., Duncan R. C., 1996, *ApJ*, 473, 322  
 Thompson C., Duncan R. C., Woods P. M., Kouveliotou C., Finger M. H., van Paradijs J., 2000, *ApJ*, 543, 340  
 Treves A., Turolla R., Zane S., Colpi M., 2000, *PASP*, 112, 297  
 Tsai W. Y., Erber T., 1975, *Phys. Rev. D*, 12, 1132  
 Tsuruta S., 1998, *Phys. Rep.*, 292, 1  
 Vasisht G., Gotthelf E. V., 1997, *ApJ*, 486, L129  
 Ventura J., 1979, *Phys. Rev. D*, 19, 1684  
 Ventura J., Nagel W., Mészáros P., 1979, *ApJ*, 233, L125  
 Virtamo J., Jauho P., 1975, *Nuovo Cimento B*, 26, 537  
 Walter F. M., Matthews L. D., 1997, *Nat*, 389, 358  
 Walter F. M., Wolk S. J., Neuhauser R., 1996, *Nat*, 379, 233  
 Yakovlev D. G., Kaminker A. D., Gnedin O. Y., Haensel P., 2001, *Phys. Rep.*, in press (astro-ph/0012122)  
 Zane S., Turolla R., Treves A., 2000, *ApJ*, 537, 387  
 Zane S., Turolla R., Stella L., Treves A., 2001, *ApJ*, submitted (astro-ph/0103316)  
 Zavlin V. E., Pavlov G. G., Shibano Yu. A., 1996, *A&A*, 315, 141  
 Zavlin V. E., Pavlov G. G., Trümper J., 1998, *A&A*, 331, 821

## APPENDIX A: NORMAL MODE POLARIZATION VECTOR FOR MAGNETIZED ELECTRON-ION PLASMA

We outline here the derivation of the polarization vector  $\mathbf{e}^j$  for a magnetized electron-ion plasma. Many previous works on opacities did not include the ion effects on the polarization vector (e.g. Ventura 1979; Mészáros 1992; see, however, Bulik & Pavlov 1996). Our derivation is patterned after Shafranov (1967) (see also Ginzburg 1970), who calculated the index of refraction but did not give the explicit expression for the polarization vector.

Neglecting the magnetic susceptibility and assuming no external charges or currents, the Maxwell equations are used to derive the equation for plane waves with  $\mathbf{E} \propto e^{i(\mathbf{k} \cdot \mathbf{r} - \omega t)}$ :

$$[\epsilon_{ij} + n^2(\hat{k}_i \hat{k}_j - \delta_{ij})]E_j = 0, \quad (\text{A1})$$

where  $\hat{k} = \mathbf{k}/k$ ,  $E_i$  and  $k_i$  are the  $i$ th component of the electric field and wavevector of the plane wave, respectively, and  $n = ck/\omega$  is the refractive index. In the frame where the external magnetic field  $\mathbf{B}$  is aligned along the  $z$ -axis, the dielectric tensor is given by

$$[\epsilon'_{ij}] = \begin{bmatrix} \epsilon & ig & 0 \\ -ig & \epsilon & 0 \\ 0 & 0 & \eta \end{bmatrix}, \quad (\text{A2})$$

where

$$\epsilon = 1 - \sum_s \frac{\lambda_s v}{\lambda_s^2 - u}, \quad (\text{A3})$$

$$\eta = 1 - \sum_s \frac{v}{\lambda_s}, \quad (\text{A4})$$

$$g = - \sum_s \frac{u^{1/2} v}{\lambda_s^2 - u}. \quad (\text{A5})$$

Here the sums run over each charged particle species  $s$  in the plasma, and  $u = \omega_{Bs}^2/\omega^2$  and  $v = \omega_{ps}^2/\omega^2$ , where  $\omega_{Bs}$  and  $\omega_{ps}$  are the cyclotron and plasma frequencies of charged particle  $s$ , respectively. Damping of the particle motion is accounted for in  $\lambda_s = 1 + i\nu_s/\omega$ , where  $\nu_s$  is the damping rate of a particle of species  $s$ . As in previous studies, damping is usually taken to be small, so that  $\lambda_s \rightarrow 1$ . In the frame where the propagation wavevector  $\mathbf{k}$  is aligned along the  $z$ -axis and  $\mathbf{B}$  is in the  $x$ - $z$  plane, the dielectric tensor is given by

$$[\epsilon_{ij}] = \begin{bmatrix} \epsilon \cos^2 \theta_B + \eta \sin^2 \theta_B & ig \cos \theta_B & (\epsilon - \eta) \sin \theta_B \cos \theta_B \\ -ig \cos \theta_B & \epsilon & -ig \sin \theta_B \\ (\epsilon - \eta) \sin \theta_B \cos \theta_B & ig \sin \theta_B & \epsilon \sin^2 \theta_B + \eta \cos^2 \theta_B \end{bmatrix}. \quad (\text{A6})$$

Substituting equation (A6) into equation (A1) and setting the determinant of the resulting equation to zero yields the index of refraction,

$$n^2 = \frac{B \pm (B^2 - 4AC)^{1/2}}{2A}, \quad (\text{A7})$$

where

$$A = \epsilon \sin^2 \theta_B + \eta \cos^2 \theta_B, \quad (\text{A8})$$

$$B = (\epsilon^2 - g^2 - \epsilon\eta) \sin^2 \theta_B + 2\epsilon\eta, \quad (\text{A9})$$

and

$$C = (\epsilon^2 - g^2)\eta. \quad (\text{A10})$$

To obtain the polarization vector, we write the electric field as  $\mathbf{E} = \mathbf{e}^j = e_0(iK_j, 1, iK_{zj})$ , where  $iK_j = E_x/E_y$ ,  $iK_{zj} = E_z/E_y$ , and  $e_0 = (1 + K_j^2 + K_{zj}^2)^{-1/2}$  from the normalization  $|\mathbf{E}|^2 = 1$ . From equation (A1), we find

$$K_{zj} = -\epsilon_{zz}^{-1}(\epsilon_{zx}K_j - i\epsilon_{zy}), \quad (\text{A11})$$

which gives equation (2.44) when considering the case of electrons and one species of ions. Equation (A1) can also be used to obtain  $K_j$ , which is given by equation (2.43), with

$$\beta = - \frac{(\epsilon^2 - g^2 - \epsilon\eta) \sin^2 \theta_B}{2g\eta \cos \theta_B}. \quad (\text{A12})$$

Specializing to the case of electrons and one species of ions, equation (A12) can be simplified to equation (2.45). Once  $\mathbf{e}^j$  is rotated into the frame with  $\mathbf{B}$  along the  $z$ -axis, the polarization vector becomes equations (2.41) and (2.42).

This paper has been typeset from a  $\text{\TeX}/\text{\LaTeX}$  file prepared by the author.